MNRAS **000**, 000–000 (2015) Preprint 21 June 2020 Compiled using MNRAS LATEX style file v3.0

Periodic X-ray Sources in the Galactic Bulge: Application of the Gregory-Loredo Algorithm

Tong Bao,[1,2]★ Zhiyuan Li,[1,2]†
[1]*School of Astronomy and Space Science, Nanjing University, Nanjing 210046, China*
[2]*Key Laboratory of Modern Astronomy and Astrophysics (Nanjing University), Ministry of Education, Nanjing 210046, China*

Accepted XXX. Received YYY; in original form ZZZ

ABSTRACT
We present the discovery of 23 X-ray periodic sources in the Limiting Window (LW), a low-extinction region in the Galactic bulge, locating 80' south of the Galactic center. Their luminosities range($10^{31} - 10^{33}$ erg s^{-1}) and period distribution(mostly between 1 to 3 hour), indicate they are cataclysmic variables (CVs). Most of them are polars with relatively harder spectrum, suggesting an unusual sub-class of mCVs. The brighter sources (6 out of 23 with L>10^{32} erg s^{-1}) in this sample are more likely IPs, with mean M_{WD} about 0.8 $M_{\odot}$. We also proved that the Gregory-Loredo (GL) method used in this work has better sensitivity and data usage compared to the Lomb-Scargle (LS) method. In combination with the simulation and the geometry of accretion in CVs, we constrain the proportion of polars to X-ray sources in LW about 17%, and the fraction of DNe is about 25%, though with more uncertainty. Still, this discovery confirms the sub-type of unusual mCVs and provides a practical way to study the population about X-ray sources based on periodic modulation.

Key words: Galaxy: bulge — X-rays: stars — X-rays: binaries

1 INTRODUCTION

X-ray-emitting, close binaries, which involve an black hole, a neutron star or a white dwarf (WD) accreting from a companion star, are among the first objects discovered in the X-ray sky and now understood to be ubiquitous in the local universe. As such, X-ray binaries can serve as a useful probe of their parent stellar populations. In particular, cCataclysmic variables (CVs), are close binary including a white dwarf (WD) and a main-sequence or sub-giant companion, whose material could be accreted by Roche-lobe overflow or stellar wind. They can be divided into magnetic (mCVs) and nonmagnetic CVs (non-mCVs) according to their magnetic field strengths of WDs. In addition, the mCVs are split into polars ($P_{spin}/P_{orb} \simeq 1$) and IPs ($P_{spin}/P_{orb} \simeq 0.01-1$), depending on their level of synchronization. The evolution of CVs are driven by angular momentum losses (AML) to keep the period from expanding, which would made system detached. The existence of "period gap" is caused by the change of mechanism for angular momentum losses. The dominant AML mechanism in long-period systems ($P_{orb} \geq 3$ hour) is "magnetic braking", whereas short-period CVs ($P_{orb} \leq 2$ hour) are driven by gravitational radiation. Meanwhile, there is a minimum period of CVs, resulted from the mass-loss-induced loss of thermal equilibrium in companion star. The orbital period of CVs are mainly between 1 to 10 hours, making it suitable for X-ray timing analysis.

It has been proved that the collective properties of CVs serve as great probe for dynamic interactions of their local environment, contributed from the high abundance of WDs in binaries. The effect would be remarkable only with extremely high stellar density (e.g. galactic center or global clusters (Cheng et al. 2019)) for us obtaining observable evidence in Hubble time. In addition to that, the individual properties of CVs provide hints for the accretion region and magnetic field, especially from their periodic variability.

It has been suggested that the thousands of X-ray sources in galactic center are magnetic cataclysmic variables, particularly intermediate polars (IPs) (Muno et al. 2009; Zhu et al. 2018). Due to the lack of optical/infrared imaging and spectroscopy resulted from high extinction and source crowding, the direct identification of them has been really difficult. In fact, even the presence and characteristics of the He II λ4686 and Hβ line have been often used to judge if a CV is magnetic or not, the proof is far from conclusive. In Silber (1992), many IPs with weak Hβ lines could not be identified from non-magnetic systems using this diagnostic. Hence the periodicity becomes a well recognized probe to study their population, because of their different features in periodic modulation (see Section 6.2).

In Muno et al. (2003), eight periodic sources were identified as mCVs in galactic center region (GCR). Then for galactic bulge region, ten periodic sources were found by using Lomb-Scargle methods (Hong et al. 2012). They were believed as an unusual type of mCVs with harder spectra like IPs while their period distribution resembles that of polars. The research was based on the observation of low-extinction Window fields (LW), locating at 1°4 south of the

★ E-mail: baotong@smail.nju.edu.cn
† E-mail: lizy@nju.edu.cn

© 2015 The Authors

Table 1. *Chandra* observations of the Limiting Window

ObsID	Start Time UT	Nominal R.A. (◦)	Nominal Decl. (◦)	Roll angle (◦)	Exposure ks	Mode
6362	2005-08-19 16:15	267.86875	-29.58800	273	37.7	FAINT
5934	2005-08-22 08:16	267.86875	-29.58800	273	40.5	FAINT
6365	2005-10-25 14:55	267.86875	-29.58800	265	20.7	FAINT
9505	2008-05-07 15:29	267.86375	-29.58475	82	10.7	VFAINT
9855	2008-05-08 05:00	267.86375	-29.58475	82	55.9	VFAINT
9502	2008-07-17 15:45	267.86375	-29.58475	281	164.1	VFAINT
9500	2008-07-20 08:11	267.86375	-29.58475	280	162.6	VFAINT
9501	2008-07-23 08:13	267.86375	-29.58475	279	131.0	VFAINT
9854	2008-07-27 05:53	267.86375	-29.58475	278	22.8	VFAINT
9503	2008-07-28 17:37	267.86375	-29.58475	275	102.3	VFAINT
9892	2008-07-31 08:07	267.86375	-29.58475	275	65.8	VFAINT
9893	2008-08-01 02:44	267.86375	-29.58475	275	42.2	VFAINT
9504	2008-08-02 21:23	267.86375	-29.58475	275	125.4	VFAINT

Galactic center. Its rarity of avoiding the obscuration from molecular cloud deserved our deeper excavation of these X-ray sources. Besides, according to RK catalog (Ritter & Kolb 2003), the mCVs (mostly DNe) occupied 20% in CVs sample, while for GCR, this fraction was reckoned over 30-40% (Hailey et al. 2016; Hong et al. 2012). The miss of non-mCVs demands reliable explanation from analyzing the properties of these sources. It may indicates that a large number of non-mCVs still awaits discovery since faint class can be always missed in flux-limited surveys.

In this work, we revisit the *Chandra* observations of the LW, employing a novel technique, known as the Gregory-Loredo period searching algorithm, to detect periodic signals in the LW. Meanwhile, the methods with more efficiency and the simulation with higher accuracy have been both operated. We explored the X-ray properties of 23 periodic sources (ten of them identified in Hong et al. (2012)). In Section 2, we describe the preparation of the X-ray data and a raw list of X-ray sources in the LW. We then provide in Section 3 a brief overview of the period searching methods, with an emphasis on the Gregory-Loredo algorithm.main methods for period finding and focuses on the GL method we adopted in this work. Section 4 is devoted to the period searching results. Section 5 presents an X-ray spectral analysis for the detected periodic sources. The comparison with previous work, the identification for these periodic sources and the X-ray source population in the LW would be discussed in Section 6. A summary of this study is given in Section 7.

2 X-RAY DATA PREPARATION

2.1 *Chandra* observations

The LW towards the inner Galactic bulge has been extensively observed by *Chandra* with its Advanced CCD Imaging Spectrometer (ACIS). A total of 13 ACIS-I observations were taken, three in 2005 and ten in 2008, resulting in a total exposure of 982 ks. A log of these observations is given in Table 1. A number of previous studies have made use of all or part of these observations, which primarily focused on the identification of discrete X-ray sources and the quantification of their statistical properties (Revnivtsev et al. 2009; van den Berg et al. 2009; Hong et al. 2009; Revnivtsev et al. 2011; Hong 2012; Morihana et al. 2013; Wevers et al. 2016).

We downloaded and uniformly reprocessed the archival data with CIAO v4.10 and CALDB v4.8.1, following the standard procedure[1]. The CIAO tool *reproject_aspect* was employed to align the relative astrometry among the individual observations, by matching the centroids of commonly detected point sources. ObsID 9502, which has the longest exposure (164.1 ks), served as the reference frame. The level 2 event file was created for each ObsID, with the arrival time of each event corrected to the Solar System barycenter (i.e., Temps Dynamique Barycentrique time) by using the CIAO tool *axbary*. We then constructed a merged event list, reprojecting all events to a common tangential point, [R.A., Decl.]=[267.86375, 29.58475]. The individual observations cover a similar field-of-view (FoV) due to their similar aimpoints and roll angles, as illustrated in Figure 1 which displays the merged 2–8 keV counts image. We have examined the light curve of each ObsID and found that the instrumental background was quiescent for the vast majority of time intervals. Hence we preserved all the science exposures for source detection and subsequent timing analysis, taking the advantage of uninterrupted signals within each observation.

2.2 Source detection

It is known that the LW suffers from moderate line-of-sight extinction, $N_{\rm H} \approx 7 \times 10^{21}$ cm^{-2} (Revnivtsev et al. 2011), which obscures X-ray photons with energies $\lesssim$ 1 keV. Here we focus on sources prominent in the 2–8 keV band, which are most likely CVs located in the Galactic bulge. This will also facilitate a direct comparison with the CVs found in the Nuclear Star Cluster (Zhu et al. 2018), the line-of-sight column density of which, $N_{\rm H} \sim 10^{23}$ cm^{-2}, is only transparent to photons with energies $\gtrsim$2 keV.

Source detection was performed following the procedures detailed in Zhu et al. (2018). Briefly, we first generated for each observation an exposure map as well as point-spread function (PSF) maps with enclosed count fraction (ECF) of 50% and 90%. Both the exposure and PSF maps were weighted by a fiducial spectrum, which is an absorbed bremsstrahlung with a plasma temperature of 10 keV and a column density of $N_{\rm H} = 10^{22}$ cm^{-2}, representative of the X-ray sources in the LW. We then reprojected the individual exposure maps to form a stacked exposure map in the same way as for the counts images; the PSF maps were similarly stacked, weighted by the corresponding exposure map. Next, we employed

[1] http://cxc.harvard.edu/ciao

wavdetect to identify discrete sources in the merged 2–8 keV counts image, supplying the algorithm with the stacked exposure map and the 50%-ECF PSF map and adopting a false-positive probability threshold of 10^{-6}. This resulted in a raw list of 847 independent sources in the 2–8 keV band.

The source centroid derived from *wavdetect* was refined using a maximum likelihood method that iterates over the detected counts within the 90% enclosed counts radius (ECR). Starting from this step we consider the 1–8 keV band to maximize the signal from potential sources in the LW. Then, for each ObsID, source counts were extracted from the 90% ECR, while background counts were extracted from a concentric annulus with inner-to-outer radii of 2–4 times the 90% ECR, excluding any pixel falling within 2 times the 90% ECR of neighboring sources. Source crowding is not a general concern in the LW, but in a few cases the source extraction region was reduced to 50% ECR due to otherwise overlapping sources. The total source and background counts were obtained by summing up the individual observations. Photometry (i.e., net photon flux and its error) for individual sources were calculated using the CIAO tool *aprates*, which takes into account the local effective exposure, background and ECF. We consider a *significant detection* for a given source in a given ObsID if the photon flux is greater than 3 times the error. We further define for each source an inter-observation *variability index*, $\mathrm{VI} = \mathrm{S_{max}}/\mathrm{S_{min}}$, where $\mathrm{S_{max}}$ and $\mathrm{S_{min}}$ are the maximum and minimum photon fluxes among all the significant detections, respectively. This implicitly requires significant detections in at least two observations.

3 PERIOD SEARCHING METHOD

In this section, we first provide our motivation of employing the Gregory-Loredo (GL) algorithm, followed by an outline of its basic principles (Section 3.1). We then describe our application of the GL algorithm to the *Chandra* data of the LW (Section 3.2). This is complemented by a set of simulations to evaluate the detection (in)completeness of periodic signals (Section 3.3).

3.1 The Gregory-Loredo Algorithm

There exists in the literature a variety of period searching methods, which can be broadly divided into three categories according to their working principles.

The most traditional method is based on Fourier transform and its power density spectra, which includes the classical Schuster periodogram (Schuster 1898), the Fourier analysis with unequally-spaced data (Deeming 1975), the correlation-based method (Edelson & Krolik 1988), among others.

Another widely-used method seeks to fit the data with a periodic model in the frequency space, employing statistics such as least-squares residuals to define the likelihood function and then selecting the frequency that maximizes the likelihood. The famous Lomb-Scargle periodogram (Lomb 1976; Scargle 1982, hereafter LS) belongs to this category. Note that when adopting trigonometric functions, the least-squares method falls into the Fourier transformation category. Another variant is to replace the least-squares residuals with polynomial fits, such as that used in Schwarzenberg-Czerny (1996).

The last category is the phase-folding method. For each trial period the time-tagged data is folded as a function of phase, and the best-fit period is found by optimizing the cost function through the frequency space. The cost function is designed to evaluate how much the phase-folded light curve deviates from constant. Methods belonging to this category use diverse cost functions. Several widely known examples are the Epoch Folding (EF) algorithm (Leahy et al. 1983), the Phase Dispersion Minimization (Stellingwerf 1978), and the GL algorithm (Gregory & Loredo 1992).

In X-ray observations, the detection of periodic signals is often involved with irregularly and sparsely sampled data. When working in frequency space, such a sampling can lead to spurious signals and hevay contamination to the real signal. Phase-folding methods, on the other hand, can avoid the effect of non-uniform data since the dead time does not enter the algorithm. Moreover, the number of detected source counts is often only moderate. While one can in principle apply binning to create photometric light curve, it takes the price of potentially losing temporal information. Phase-folding methods, on the other hand, directly handle individual events, thus maximally incorporating the temporal information.

Most X-ray sources in the LW share the characteristics of irregular sampling and limited source counts. Therefore, it is appropriate to employ the GL algorithm, which applies the Bayesian probability theory to the phase-folded light curve, to search for periodic signals for the LW sources. We provide a brief overview of Bayes's theorem and the GL algorithm in Appendix A. The key of this algorithm is the multiplicity of the phase distribution of events,

$$W_m(\omega, \phi) = \frac{N!}{n_1!\, n_2!\, n_3! \cdots n_m!}. \tag{1}$$

Here N represents the total number of counts of a given source, $n_i(\omega, \phi)$ is the number of events falling into the ith of m phase bins given the frequency ω and the phase ϕ, satisfying $\sum_{i=1}^{m} n_i(\omega, \phi) = N$. The multiplicity is the number of ways that the binned distribution could have arisen by chance. It can be easily shown that the more the values of n_i differ from each other, the smaller the multiplicity. In other words, the more the piecewise model defined the m phase bins deviates from constant, the more likely there exists a periodic signal, the probability of which is inversely proportional to the multiplicity.

In general, the GL algorithm takes the following steps:

(i) Compute the multiplicity for all sets of (m, ω, ϕ) (Eqn. 1). In this work, the highest value of m is set to be 12.

(ii) Given m, integrate over the (ω, ϕ) space and calculate the so-called "odds ratio" using Bayes's theorem (Eqn. A16). The "odds ratio" determines the ratio of probabilities between a periodic model and a non-periodic (constant) model.

(iii) Sum up the normalized odds ratios of each m to determine the probability of a periodic signal (Eqn. A20). If this probability exceeds a predefined threshold (for instance, 90%), a periodic signal is favored.

(iv) Finally, compare all the odds ratios integrated over the ϕ space, finding the value of ω with the highest odds ratio, which then gives the period $P = 2\pi/\omega$ (Eqn. A21).

3.2 Application to the LW

We apply the GL algorithm to search for periodic signals in the LW sources. For a given source, the 1–8 keV counts within the 90% ECR of individual ACIS-I observations are extracted to form a time series. In addition, we supply for each source the information of "epoch", i.e., the start time and end time of each ObsID in which the source has at least one detected count. This information is used to compensate for the uneven distribution over the phase bins (see Eqn. A17 for a detailed illustration). Since the GL algorithm determines the probability of a periodic signal against a constant

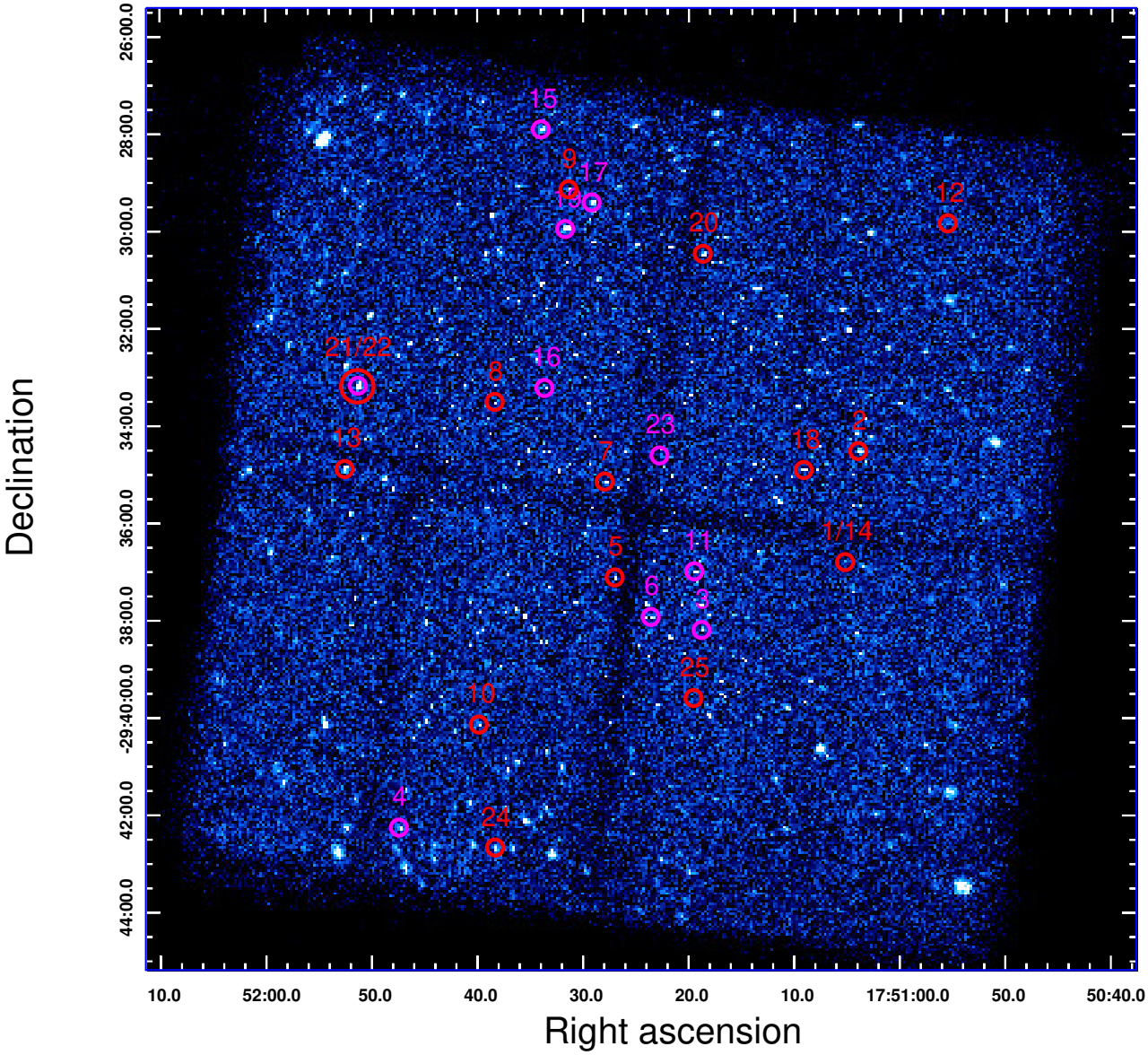

Figure 1. 2–8 keV counts image of the Limiting Window, combining 13 *Chandra*/ACIS-I observations. Locations of the 23 periodic sources are marked with colored circles (*magenta*: ten sources previously reported by Hong et al. 2012; *red*: thirteen newly discovered in this work). Source numbering is the same as in Table 2. In particular, 1/14 and 21/22 are the two sources each showing two periodic signals.

light curve, there is no need to separately account for the background level, which is absorbed into the constant. Nevertheless, we have measured the local background (Section 2.2) for each periodic source as a consistency check (see Section 4).

As mentioned in Section 3.1, the GL algorithm folds the time series at a trial frequency (or period). In practice, the resolution and range of frequency must be compromised between accuracy and computational power. Thus we restrict our analysis on three period ranges: (300, 3000), (3000, 10000) and (10000, 50000) sec, with a frequency resolution of 10^{-7}, 10^{-8} and 10^{-9} Hz, respectively. The period ranges are chosen based on the expectation that most, if not all, detectable periodic X-ray sources in the LW should be CVs. The orbital period distribution of CVs is known to exhibit a minimum at about 82 minutes, a gap between 2–3 hours, and a maximum around 10 hours (Ritter & Kolb 2003). The second and third period ranges well cover these characteristic periods, whereas the first range probes the spin period of fast rotating IPs. Given the timespan of $\sim 10^8$ sec between the first and last ACIS-I observations, the chosen frequency resolutions are optimal for an efficient search of periodic signals.

3.3 Detection completeness

For a given period searching algorithm, the detection rate depends on both the number of observed counts, the intrinsic shape of the light curve, as well as the observing cadence. To quantify the detection rate and hence gain insight on the nature of the periodic sources in the LW, we perform simulations following the merit of Cicuttin et al. (1998). Two functional forms of light curve are considered: a sinusoidal function and a piecewise function. While these are admittedly idealized shapes, they can represent realistic light curves,

e.g., the former resulted from rotational modulation and the latter due to eclipse.

A sinusoidal light curve follows,

$$\lambda(t) = \lambda_0[1 + A_0 \sin(\omega t + \phi)], \quad (2)$$

where $\omega = 2\pi/P$, A_0 is the relative amplitude of variation, and λ_0 is the mean count rate which may include contribution from a constant background. The phase ϕ can be arbitrarily set at zero. For a direct comparison with observations, we relate λ_0 with the total number of counts, $C = \lambda_0 T$, where T is the exposure time of a given observation. This holds since T is typically much longer than the modulation period (P). The simulations are run with a selected number of parameters due to constraints in computational power. Specifically, we adopt C=50, 100, 200, 300, 400 and 500, A_0=0.5, 0.6, 0.7, 0.8 and 0.9, and P=554, 5540 and 45540 sec, resulting in a total of 6x5x3=90 combinations. The chosen periods are representative of the actually searched ranges (Section 3.2), whereas the adopted total counts well sample the range of observed counts from the LW sources.

We thus simulate 100 light curves for each combination of parameters, taking into account Poisson errors and the exact start and end times of the 13 ACIS-I observations. The arrival time of each simulated count is further randomly modified by an amount of 3.2 sec to mimic the effect of ACIS frame time. The simulated light curve is then searched for a periodic signal using the GL algorithm in the same manner as for the real data (Section 3.2). We count a valid detection if the found period has a detection probability greater than 90% and its value consistent with the input period to within 1%. We notice that in a small fraction of simulated light curves of the shortest input period (554 sec), the second harmonics (i.e., 2 times the true period) is detected with an even higher probability than the true period. We also consider such cases a valid detection as long as the true period itself fulfills the above criteria.

The detection rate for a given combination of parameters is taken to be the fraction of the 100 simulated light curves having a valid detection. The top, middle and bottom panels of Figure 2 show the result of the three test periods, respectively, in which several trends are apparent. First and intuitively, for a given period and amplitude, higher total counts would lead to higher detection rates, while for given total counts, a higher amplitude also leads to a higher detection rate. The simulation results confirm these expectations. Second, for the same total counts and amplitude, the detection rate is generally higher for a longer period. This can be understood as due to a statistical behavior in the multiplicity (see Eqn. 1), which has a lower value for a long period. This holds for both the sinusoidal and piecewise light curves. Lastly, for total counts of 50, the detection rate is almost always below 10% regardless of the period and amplitude.

The piecewise function, which mimics an eclipse against an otherwise constant flux, takes the form of

$$\lambda(t) = \begin{cases} \lambda_0 & \phi(t) \in [0, (1-w)\pi) \cup ((1+w)\pi, 2\pi], \\ f\lambda_0 & \phi(t) \in [(1-w)\pi, (1+w)\pi], \end{cases} \quad (3)$$

where w accounts for the eclipsing width (duration) in phase space, and f characterizes the relative depth of the eclipse ($0 \leq f \leq 1$; $f = 0$ corresponds to total eclipse). Here the middle of eclipse is assumed to occur at $\phi = \pi$. Again, λ_0 can be related to the total counts as $C = [1-(1-f)w]\lambda_0 T$. We set $f = 0.1$ and $w = 0.1$ in our simulations, which are not atypical of eclipsing CVs. We test three values of the period, P=5258, 15258 and 45258 sec and adopt trial count rates $\lambda_0 = 1, 2, 3, 4, 5, 6, 7, 8, 9, 10, 15$ and 20×10^{-4} cts s^{-1}.

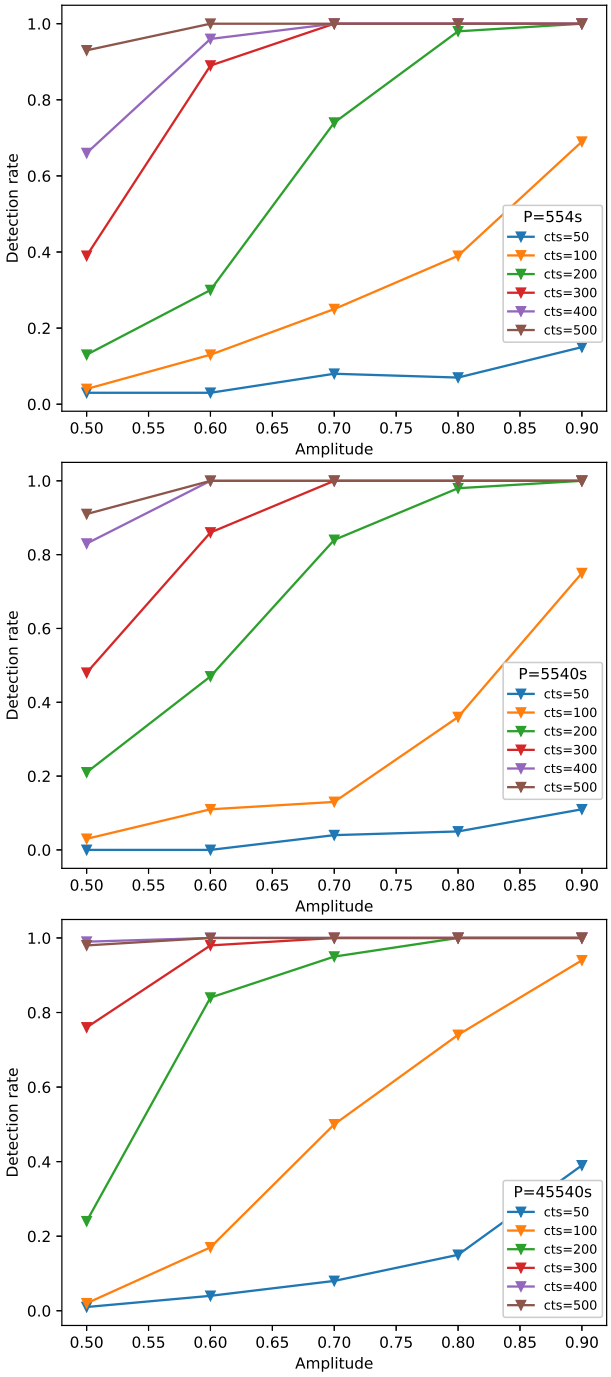

Figure 2. Detection rates as a function of relative variation amplitude, based on simulated sinusoidal light curves. The top, middle and bottom panels are for modulation period of 554, 5540 and 45540 sec, respectively. The different colored lines represent different values of total counts, as labeled. See text for details.

For each combination of parameters, 100 simulated light curves are again generated and fed to the GL algorithm. The resultant detection rate (also taking 90% as the threshold) is shown in Figure 3. As expected, the detection rate is generally higher for a longer period. It can also be seen that for total counts below ~300, the detection rate is $\lesssim$10% regardless of the period; only when total counts exceed ~1500, the detection rate becomes 100% for all test periods. Since only a small fraction of sources in the raw list have total counts more

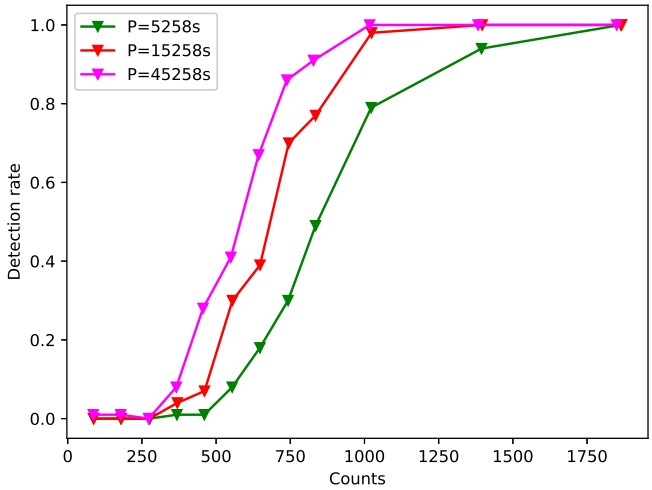

Figure 3. Detection rates as a function of total counts, based on simulated piecewise light curves. Different colored lines represent different periods, as labeled. See text for details.

than 1500, we expect a relatively low detection rate of eclipsing sources in the LW.

We have also run simulations to estimate the rate of false detection, which refers to the detection of a periodic signal from an intrinsically constant light curve. Considering that most LW sources can have a low-amplitude long-term variation, we approximate a semi-constant light curve with a sinusoidal function with P=5 yr and A_0=0.5. Simulated light curves are generated with totals counts from 50 to 5000 and fed to the GL algorithm. No false detection of periodic signals, at any value between 300–50000 sec, is found. Therefore, it seems safe to conclude that the false detection rate is essentially zero for the GL algorithm applied to the LW data.

4 PERIOD SEARCHING RESULTS

According to the simulations in Section 3.3, a periodic signal is hard to detect in LW sources with total counts $C < 100$, even in the case of high variation amplitudes. Therefore, we restrict our period searching to sources with $C \geq 100$, which include 667 of the 847 sources in the raw list. **Among these 667 sources, ??% (??%) have total counts more than 500 (1000).**

Adopting a probability threshold of 90%, we obtain 48 tentative periodic signals from the three period ranges. However, it is necessary to filter spurious detections, which may be caused by several effects:

(i) By design, the ACIS is dithered to distribute photons over more CCD pixels to avoid pile-up and to fill CCD gaps. The dither period is 706.96 s in pitch and 999.96 s in yaw. Any signal detected at these two periods and their harmonics are thus excluded. These are mostly found in sources located close to CCD gaps, where dithering significantly reduces the number of detected counts in a periodic fashion.

A related concern is how dithering would affect the detection of genuine periods. We run simulations to test this effect. Specifically, we generate simulated sinusoidal light curves with P = 5072.97 sec and C = 293. This choice is motivated by one particular periodic source (#5 in Table 2), which has a fractional detector coverage of 0.74 (in other words, 26% of the intrinsic flux is lost due to dithering into the CCD gap), the lowest among all valid periodic sources (see below). The dithering effect is mimicked by artificially removing the simulated counts according to a probability distribution calculated by the CIAO tool *dither_region*. No difference is found in the resultant detection rate, compared to that without dithering.

(ii) In certain sources, multiple detections can be caused by second and third harmonics of the same intrinsic signal (i.e., 2 and 3 times the true period). These can be easily identified by the sign of double-peak or triple-peak in the phase-folded light curve, provided that the intrinsic signal has a single-peak structure.

However, the intrinsic structure might be double-peaked, in which case it is more difficult to distinguish between the true period and the half harmonic (i.e., half the true period), in particular when the two peaks have a similar strength and width. Generally speaking, the double-peaked shape only occurs in IPs with an accretion column over each magnetic pole. When viewed from certain angle, the two poles alternatively drift across the front side of the WD, producing the double-peaked X-ray light curve. The modulation period in this case must be the spin period of the WD, typically under one hour. Among our tentative detections, most of those showing a double-peaked light curve have a corresponding period longer than 3 hours, far beyond the range of spin periods in IPs. These are probably second harmonics rather than a genuine spin period. Hence we assume that there is no half harmonics in the LW sources and always take the lowest period as the true period. This assumption is supported by our extensive simulations presented in Section 3.3, in which no half harmonic (the true period is known before hand) is found.

(iii) Strong flux variations or outbursts occupying one particular observation can also cause a false periodic signature. This is because the GL algorithm, which analyzes the phase-folded light curve, can be fooled if there were too many photons found in a single observation, producing excess in certain phase bins. In this case the algorithm may "think" there exists a period especially in the period range of (10000, 50000) sec. Among the sources with tentative periods, four exhibit a variability index VI> 10, indicating strong variations. We thus reanalyze their light curves using two subsets of observations: those covering only the outburst and those excluding the outburst. For three of them, the tentative period cannot be recovered in either subset. Therefore, these three are probably fake signals. The remaining source is retained since its period can be recovered in both the outbursting and quiescent subsets.

The above filtering thus results in 25 valid periodic signals in 23 sources. Among them, 10 signals were previously reported by Hong et al. (2012) and are confirmed here with the GL algorithm, while the remaining 15 periods are new discoveries (a comparison between our work and Hong et al. 2012 is further addressed in Section 6.1). The basic information of these periodic sources are listed in Table 2, sorted by the order of increasing period. The source locations are marked in Figure 1.

Two sources each exhibit two different periods, hence we have assigned each of them two IDs: #1/#14 and #21/#22. The phase-folded light curves at the two modulation periods are shown for source #1/#14 in the upper panels of Figure 4 and for source #21/#22 in the upper panels of Figure 5. The number of phase bins, between 20 to 50, is chosen to optimally display substructures in the light curve. While the GL algorithm does not rely on quantifying the local background, for comparison we plot in these panels the estimated background level (yellow strip, the width of which represents 1 σ Poisson error; Section 2.2). We defer discussions on the shape of the light curve, which contains important information on the nature of the periodic sources, to Section 6.2.

The phase-folded light curves are complemented by the long-term, inter-observation light curve, shown in the lower left panel of

Table 2. Information on the periodic X-ray sources in the Limiting Window

ID LW (1)	R.A. ° (2)	Decl. ° (3)	Period s (4)	Prob. (5)	C (6)	VI (7)	H-ID % (8)	$P_{\rm det}$ (9)	Harmonics (10)	Class (11)
1†	267.77173	-29.61332	853.83	0.90277	202	1.92	-	-	-	IP
2	267.76657	-29.57529	3820.83	0.99222	902	1.94	-	-	-	IP?
3	267.82829	-29.63660	4728.90	1.00000	394	2.13	H6	99	Third	IP?
4	267.94766	-29.70427	4886.79	0.99994	784	1.90	H8	98	-	polar?
5	267.86255	-29.61859	5072.97	0.99933	293	2.34	-	-	Second	polar?
6	267.84831	-29.63212	5130.57	1.00000	437	2.51	H2	100	Second	polar?
7	267.86651	-29.58575	5144.97	0.99880	335	2.48	-	-	Second	IP?
8	267.90982	-29.55845	5158.75	1.00000	121	2.30	-	-	Second	polar?
9	267.88075	-29.48562	5231.49	0.94949	347	1.65	-	-	-	polar?
10	267.91616	-29.66900	5252.93	0.91425	211	-	-	-	-	polar?
11	267.83116	-29.61651	5261.93	1.00000	438	1.46	H10	31	Second	IP?
12	267.73141	-29.49721	5334.76	0.99952	760	1.25	-	-	Second	polar?
13	267.96901	-29.58142	5501.16	0.99094	512	2.89	-	-	-	polar?
14†	267.77173	-29.61332	5608.21	0.96821	202	1.92	-	-	Third	IP
15	267.89161	-29.46508	6335.85	1.00000	823	2.09	H5	100	Second	polar?
16	267.89024	-29.55369	6597.55	1.00000	487	4.30	H9	99	Second	polar?
17	267.87162	-29.49011	7448.98	0.99999	535	1.76	H3	100	Second	polar?
18	267.78806	-29.58177	7756.19	0.99941	214	4.76	-	-	Second	IP?
19	267.88203	-29.49922	8546.28	1.00000	3402	3.27	H4	93	Second	IP?
20	267.82785	-29.50770	8844.82	0.90987	263	1.82	-	-	Second	IP?
21‡	267.96375	-29.55290	9877.52	0.99992	1963	1.44	-	-	-	IP
22‡	267.96375	-29.55290	10342.30	1.00000	1963	1.44	H1	99	-	IP
23	267.84487	-29.57680	12002.70	1.00000	307	1.86	H7	100	Second	polar?
24	267.90974	-29.71112	42219.03	1.00000	1039	23.6	-	-	-	polar?
25	267.83142	-29.65992	47317.12	0.98850	138	-	-	-	-	AB

Notes: (1) Source sequence number assigned in the order of increasing period. The same source with dual periods is marked by † and ‡. (2) and (3) Right Ascension and Declination (J2000) of the source centroid. (4) The modulation period determined by the GL algorithm. (5) The probability of the periodic signal defined by Eqn. A20. (6) The number of total counts in the 1-8 keV band. (7) The long-term variability index, defined as VI = $S_{\rm max}/S_{\rm min}$, where $S_{\rm max}$ and $S_{\rm min}$ are the maximum and minimum photon fluxes among all the valid detections. Sources #10 and #25 have no measurable VI. (8) The ID of previously detected periodic signals as given table 2 of Hong et al. (2012). (9) The detection probability with the GL algorithm based on simulated sinusoidal light curves. (10) Significant harmonics, when present. (11) Source classification based on the phase-folded light curve.

Figures 4 and 5, and by the source spectrum (see Section 5), shown in the lower right panel of Figures 4 and 5. Similar figures of the remaining 21 sources are presented in Appendix B.

5 X-RAY SPECTRAL ANALYSIS

We perform spectral analysis for all 23 confirmed periodic sources to gain insight on their nature. Source and background spectra are extracted from the same regions as described in Section 2.2, along with the ancillary response files (ARFs) and redistribution matrix files (RMFs), by using the CIAO tool *specextract*. The spectra from individual observations are then coadded to form a combined spectrum of a given source, with the corresponding ARFs and RMFs weighted by the effective exposure. Further, the spectrum is adaptively binned to achieve a minimum of 20 counts and a signal-to-noise ratio greater than 2 per bin.

The resultant spectra are analyzed using XSPEC v12.9.1. Since these sources are expected to be CVs, we adopt a fiducial spectral model (Zhu et al. 2018; Xu et al. 2019), which consists of a bremsstrahlung continuum and three Gaussian lines centered at 6.40, 6.68 and 6.97 keV, all these components subject to an unknown line-of-sight absorption (*phabs* in XSPEC). The three lines (hereafter referred to as the 6.4, 6.7 and 7.0 keV lines) correspond to neutral Fe Kα, Fe XXV Kα and Fe XXVI Lyα, respectively, which are among the most commonly detected emission lines in CV spectra. The latter two lines, in particular, arise from the post-shock plasma near the WD surface, and their flux ratio ($I_{7.0}/I_{6.7}$) has proven to be a robust tracer of the plasma temperature, hence also a good indicator of the WD mass (Xu et al. 2016).

It turns out that the plasma temperature ($T_{\rm b}$) is not well constrained in most sources, due to a moderate number of counts and the insufficient sensitivity of *Chandra* at energies above 8 keV. Hence for such cases we fix $T_{\rm b}$ at 40 keV, which is typical of IPs when their hard X-ray (up to tens of keV) spectra are available (Xu et al. 2016; Hailey et al. 2016). Setting a lower value of $T_{\rm b}$, for instance, at 20 keV, does not affect our following conclusions.

Again due to the limited number of counts, most of the periodic sources show weak or non-detected Fe lines. We have applied a bootstrapping method using the *multifake* tool in XSPEC to derive the 90% confidence range for the fluxes of the three Fe lines. It turns out that only one sources, #21 (same as #22), shows a significant line at both 6.7 keV and 7.0 keV. The flux ratio and its 90% error are similarly determined for this sources, resulting in $I_{7.0}/I_{6.7} = 0.91^{+1.22}_{-0.56}$ for #21. According to the empirical line ratio–WD mass ($I_{7.0}/I_{6.7}$–$M_{\rm WD}$) relation of Xu et al. (2019), which is calibrated with CVs in the solar neighborhood, we can infer $M_{\rm WD} \approx 0.8\ (1.2)\ M_\odot$ for #21, provided that both sources are IPs (DNe). It is noteworthy that there

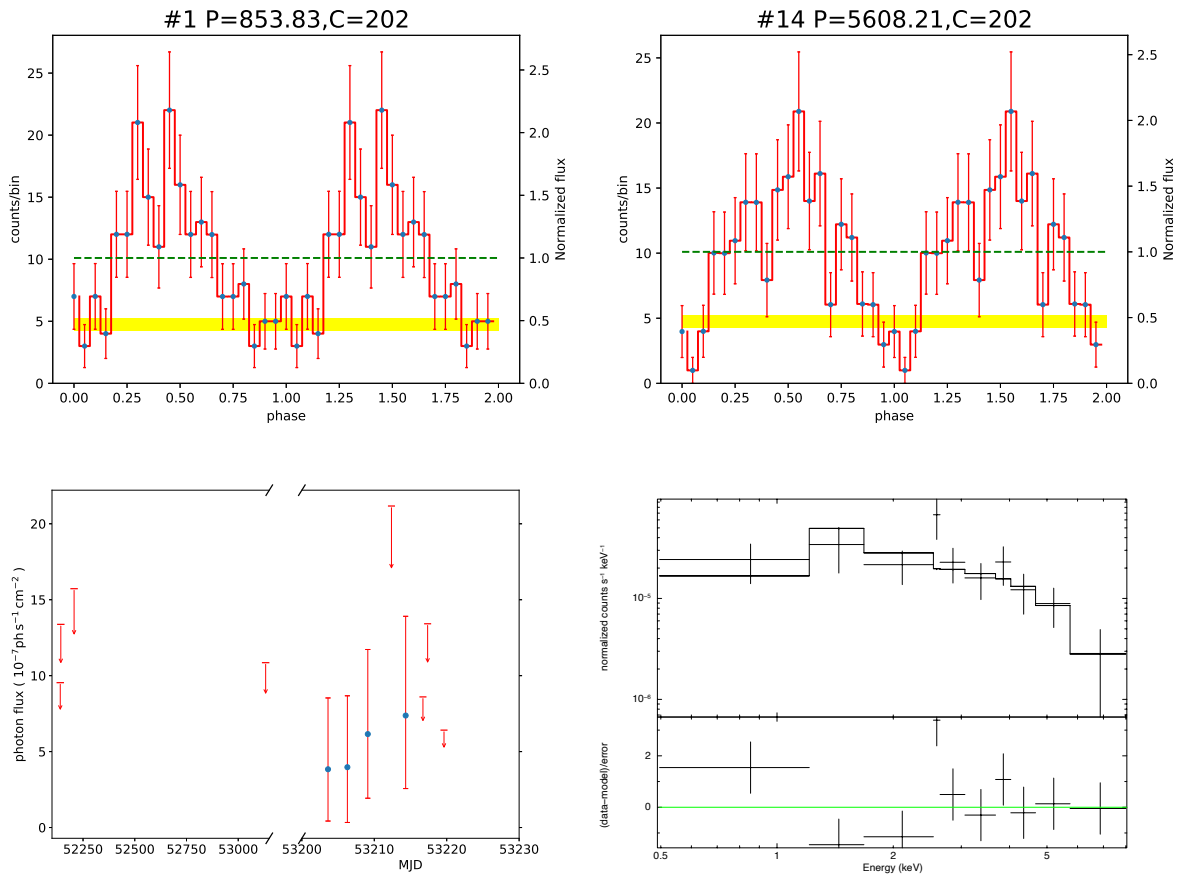

Figure 4. *Upper panels*: The 1–8 keV phase-folded light curves of source #1/#14 at the two modulation periods. The green dashed line represents the mean count rate, whereas the yellow strip represents the local background, the width of which represents 1 σ Poisson error. *Lower left*: the 1–8 keV long-term, inter-observation light curve. Arrows represent 3 σ upper limits. *Lower right*: Source spectrum and the best-fit model. See text for details.

exists no empirical $I_{7.0}/I_{6.7}$–$M_{\rm WD}$ relation for polars, mainly due to the small number of known polars in the solar neighborhood (Xu et al. 2019).

We further generate the cumulative spectrum for all sources with the exception of #21(22) and #25, since the former may dominate the iron line emission and the latter is classified as an AB (see in Section 6.2). This group has $I_{7.0}/I_{6.7} \sim 0.19$, thus inferring a mean WD mass of $M_{\rm WD} \approx$? (?) $M_\odot$ if they are IPs (DNe).

Results of the above spectral analysis are summarized in Table 3.

6 DISCUSSION

In this section, we discuss the most significant implications of our results. We first provide a comparison between our work and Hong et al. (2012) (Section 6.1). Then, we try to classify the periodic sources based on their temporal and spectral properties, demonstrating that the majority of these sources are most likely magnetic CVs (Section 6.2). Lastly, we assess the potential sub-populations of CVs in the Galactic bulge (Section 6.3).

6.1 Comparison with previous work

We have detected 25 periodic signals from 23 sources in the LW (Table 2). Our detections fully recover the 10 periodic signals from 10 sources found by Hong et al. (2012). As illustrated in the upper panel of Figure 6, the measured periods between the two methods agree with each other to within 0.7% and show no systematic bias. The remaining 15 periods are new detections. Since Hong et al. (2012) and this work have used the same set of *Chandra* observations, this difference must be owing to the different period searching methods employed.

Hong et al. (2012) employed the LS periodogram, which, as described in Section 3.1, handles the photometric light curve, while the GL algorithm processes the phase-folded light curve with tolerance for observing gaps. We have applied the LS periodogram to our data in essentially the same way as Hong et al. (2012) and confirmed that only those 10 periods found in their work can be detected by this method. The other 15 periods do not result in a significant detection in the LS periodogram, mainly due to its low efficiency with low-count sources. The detection rate is essentially zero for net counts $\lesssim$100 and never exceeds 20% for net counts of 150, according to the simulations presented in Hong et al. (2012, figure 7 therein).

For comparison, we provide an estimate on the detection rate of the 10 commonly detected periodic signals using the GL al-

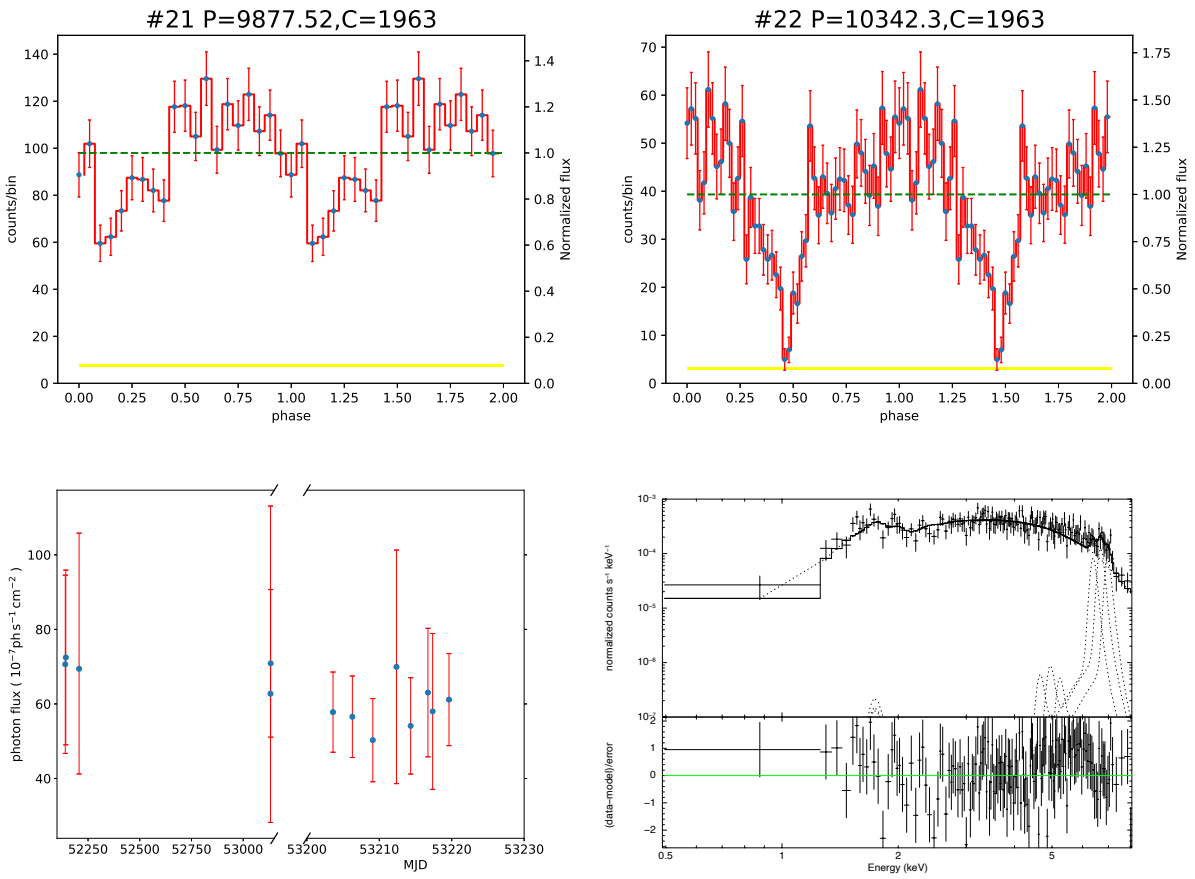

Figure 5. Similar to Figure 4, but for source #21/#22.

gorithm. For practical purposes we assume an intrinsic sinusoidal shape (Eqn. 2), for which the total counts and period are taken directly from the observed values, whereas the relative amplitude (A_0) is taken from Hong et al. (2012), which was based on the Rayleigh statistics (Buccheri et al. 1983; Muno et al. 2003). For each of the 10 signals, 100 simulated light curves are produced and fed to the GL algorithm. Again, we take the 90% probability threshold and a period accuracy of 1% to define a valid detection. The percentage of valid detections, $P_{\rm det}$ (also listed in column 9 of Table 2), is plotted in the upper panel of Figure 6, along with the detection rate of the LS periodogram taken from Hong et al. (2012). Clearly, the GL algorithm works better in almost all cases compared to the LS periodogram.

6.2 Classifying the periodic X-ray sources

While it is generally difficult to unambiguously identify the nature of an X-ray source without knowing its optical counterpart, which is the case for most LW sources, the X-ray temporal and spectral properties of the 23 periodic sources contain useful information that actually allow for a reasonable classification for many of them. First of all, all but one (#25) of these sources are found in the 1–8 keV luminosity range of 10^{31} – 10^{33} erg s^{-1} (Table 3), which is typical of CVs. On the contrary, coronally active binaries (ABs), which are thought to dominate the number of detectable X-ray sources in the LW (Revnivtsev et al. 2009), generally have unabsorbed X-ray luminosities below 10^{31} erg s^{-1} (Sazonov et al. 2006). This stems from the empirical fact that the coronal X-ray emission from low-mass stars saturates at $\sim 10^{-3}$ of the bolometric luminosity (Güdel 2004). The X-ray spectra of these sources are less informative, since except in one case (#21/#22) they lack the unambiguous sign of Fe lines due to the moderate S/N (Section 5), which otherwise would be another characteristic signature of CVs (e.g., Xu et al. 2016). Nevertheless, most of these sources do show a very hard continuum that are again typical of CVs, although this could be partly owing to the fact that our parent source list is based on the 2–8 keV band (Section 2.2). Furthermore, the vast majority of the detected periods fall between 1.1–3.3 hours, roughly overlapping with the well-known orbital minimum and the orbital gap populated by CVs in the solar neighborhood (Ritter & Kolb 2003), as illustrated in Figure 7. Therefore, the global X-ray properties point to CVs dominating the detected periodic sources, a conclusion also drawn by Hong et al. (2012).

It will then be interesting to ask to which sub-class of CVs these periodic sources belong. The phase-folded light curves may provide useful hints to this question. In magnetic CVs, including polars and IPs, their orbital and spin modulations can give rise to a complex light curve. For polars, let us consider the simplistic situation in which hard X-rays (photon energy $\gtrsim$1 keV) are produced in only one of the two magnetic poles[2]. Denoting i the angle between the line-of-sight and the spin axis, β the angle between the spin and magnetic

[2] In this picture, accretion can still take place in the other pole, in fact, at a

Table 3. X-ray spectral properties of the periodic sources

ID	$N_{\rm H}$	$T_{\rm b}$	$EW_{6.7}$	χ^2/dof	L_{1-8}
(1)	(2)	(3)	(4)	(5)	(6)
LW	10^{22} cm^{-2}	keV	keV		10^{31} erg s^{-1}
1†	$0.51^{+0.75}_{-0.34}$	40 (fixed)	<7.44	1.14/5	$2.02^{+0.71}_{-0.57}$
2	$2.17^{+0.54}_{-0.46}$	$20.7^{+56.9}_{-9.92}$	<1.28	0.86/78	$25.7^{+3.00}_{-2.24}$
3	$1.34^{+0.70}_{-0.40}$	$46.4^{+46.1}_{-38.5}$	<1.37	0.98/33	$7.34^{+1.17}_{-0.86}$
4	$1.15^{+0.69}_{-0.50}$	$11.3^{+53.3}_{-4.71}$	<0.96	0.91/27	$25.0^{+3.27}_{-4.91}$
5	$1.02^{+0.27}_{-0.23}$	40 (fixed)	<1.22	1.00/33	$6.21^{+0.86}_{-0.78}$
6	$1.82^{+0.57}_{-0.50}$	$6.90^{+12.4}_{-2.90}$	<1.77	1.12/42	$10.3^{+1.38}_{-1.23}$
7	$1.62^{+0.62}_{-0.49}$	$41.6^{+43.0}_{-32.3}$	< 1.26	0.86/39	$7.45^{+0.99}_{-0.90}$
8	$2.06^{+1.51}_{-0.94}$	40 (fixed)	< 4.89	0.93/7	$1.96^{+0.60}_{-0.47}$
9	$1.29^{+1.34}_{-0.67}$	$20.8^{+95.8}_{-20.8}$	<2.44	1.10/7	$3.88^{+1.36}_{-0.96}$
10	$2.50^{+7.25}_{-1.56}$	40 (fixed)	<7.29	0.85/5	$2.38^{+1.96}_{-0.84}$
11	$1.85^{+0.39}_{-0.33}$	40 (fixed)	<1.10	1.22/47	$10.5^{+1.24}_{-1.14}$
12	$6.23^{+9.67}_{-3.66}$	40 (fixed)	-	0.78/6	$8.42^{+6.40}_{-3.25}$
13	$0.90^{+0.30}_{-0.24}$	40 (fixed)	<2.27	1.15/38	$9.43^{+1.25}_{-1.16}$
14†	$0.51^{+0.75}_{-0.34}$	40 (fixed)	<7.44	1.14/5	$2.02^{+0.71}_{-0.57}$
15	$1.46^{+0.48}_{-0.38}$	40 (fixed)	<2.12	1.16/42	$14.3^{+1.97}_{-1.79}$
16	$0.89^{+0.18}_{-0.16}$	40 (fixed)	<1.25	1.43/51	$9.41^{+0.98}_{-0.92}$
17	$2.68^{+0.63}_{-0.52}$	40 (fixed)	<2.87	0.75/36	$12.5^{+1.78}_{-1.61}$
18	$2.01^{+0.92}_{-0.66}$	40 (fixed)	<2.03	0.53/14	$4.68^{+0.99}_{-0.85}$
19	$1.82^{+0.10}_{-0.10}$	40 (fixed)	$0.049^{+0.150}_{-0.044}$	0.95/185	$93.2^{+3.61}_{-3.51}$
20	$2.09^{+2.45}_{-1.16}$	$4.04^{+28.2}_{-2.54}$	<5.26	1.04/12	$5.99^{+2.01}_{-1.64}$
21‡	$2.83^{+0.25}_{-0.23}$	40 (fixed)	$0.23^{+0.44}_{-0.18}$	1.10/147	$66.7^{+3.61}_{-3.47}$
22‡	$2.83^{+0.25}_{-0.23}$	40 (fixed)	$0.23^{+0.44}_{-0.18}$	1.10/147	$66.7^{+3.61}_{-3.47}$
23	$1.83^{+0.44}_{-0.37}$	40 (fixed)	<1.86	1.47/35	$10.3^{+1.36}_{-1.25}$
24	$0.35^{+0.16}_{-0.13}$	$4.78^{+3.55}_{-1.58}$	<2.39	1.19/55	$9.70^{+1.22}_{-1.09}$
25	$0.83^{+3.31}_{-0.83}$	$2.30^{+1.59}_{-0.85}$	-	0.80/2	$0.84^{+0.34}_{-0.31}$
AG	$1.40^{+0.07}_{-0.07}$	40 (fixed)	$0.18^{+0.07}_{-0.03}$	1.04/205	$12.0^{+0.32}_{-0.32}$

Notes: (1) Source sequence number as in Table 2. And "CV" denotes for the combined spectra of all periodic sources except for #21(22) and #25. †Sources 1 and 14 are the same source with two different periods; ‡Sources 21 and 22 are the same source with two different periods. (2) Line-of-sight absorption column density. (3) The bremsstrahlung temperature, in units of keV. Fixed at a value of 40 keV when the spectrum provides no signficant constraint to this parameter. (4) Equivalent width of 6.7 keV line.
(7) χ^2 and degree of freedom of the best-fit model. (8) 1–8 keV unabsorbed luminosity. Quoted errors are at the 90% confidence level.

axes, and ϵ the magnetic colatitude of the accretion column, when $i+\beta+\epsilon > 90^{\circ}$, the two poles will alternately drift across the front side of the WD. The resultant light curve will look like that of source #6 , #8 and #10, with nearly half of the cycle showing no significant hard X-ray emission (Heise et al. 1985). The periods of these sources are consistent with the period range of known polars (for polars the orbital and spin periods are equal; Figure 7). This so-called "two-pole" behavior becomes more complicated if hard X-rays were produced near both poles, in which case the second pole can partially fill the dip, resulting in a light curve like that of #4, #5, #9, #12, #13, #15 ,#16, #17, #23 and #24. On the other hand, if $i+\beta+\epsilon < 90^{\circ}$ and $\beta < i$, the hard X-ray-emitting pole would be always visible (so-called "one-pole" behavior), producing a roughly constant light curve, although at certain phase dips can still present due to obscuration by the accretion stream.

IPs share the above two-pole or one-pole behavior. In addition, the orbital modulation can result in eclipse of the WD by the companion star (Hellier et al. 1993), by the accretion stream, or by the "disc overflow" (Norton et al. 1996). Thus the light curve shape of IPs are complex and can exhibit both sinusoidal variations and dips, Examples of this kind are found in sources #3, #7, #11, #18 and #20. In addition, source #19, which has the highest X-ray luminosity (9.3×10^{32} erg s^{-1}) with only moderate sinusoidal variation, is most likely the orbital modulation of an IP.

The most robust identification of IPs is to detect both the spin and orbital periods. Among our sources, #1 (#14) and #21 (#22) show two different periods. For #1, the period is 853.8 sec and the

much higher accretion rate, producing quasi-black-body emission peaking at the soft X-ray and extreme ultraviolet bands (Hellier 2001).

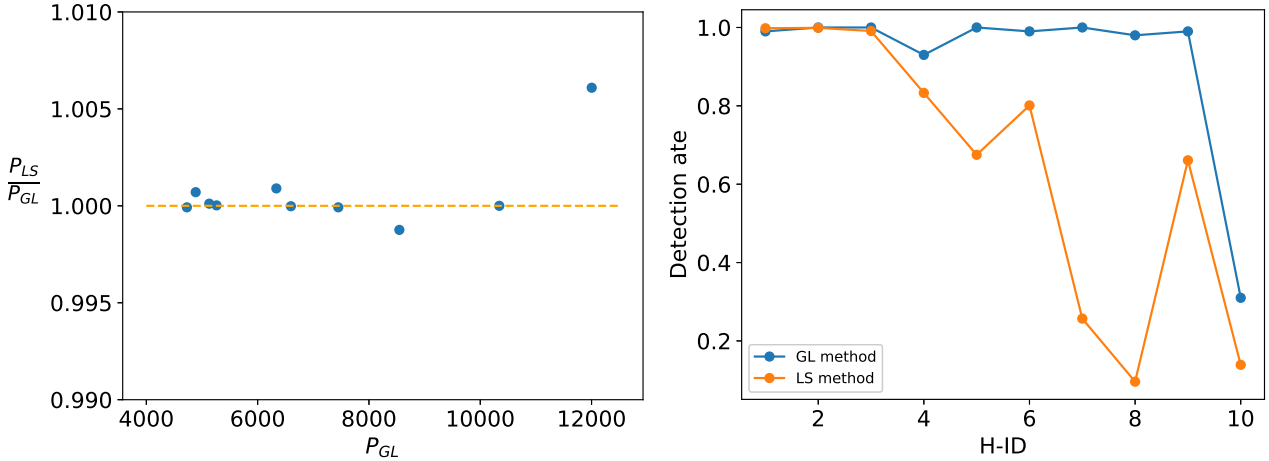

Figure 6. Comparison between the periods (*left*) and detection rate (*right*) of the 10 signals commonly found by the GL and LS methods.The H-ID is the sequence number given in Hong et al. (2012), same as listed in column 6 of Table 2.

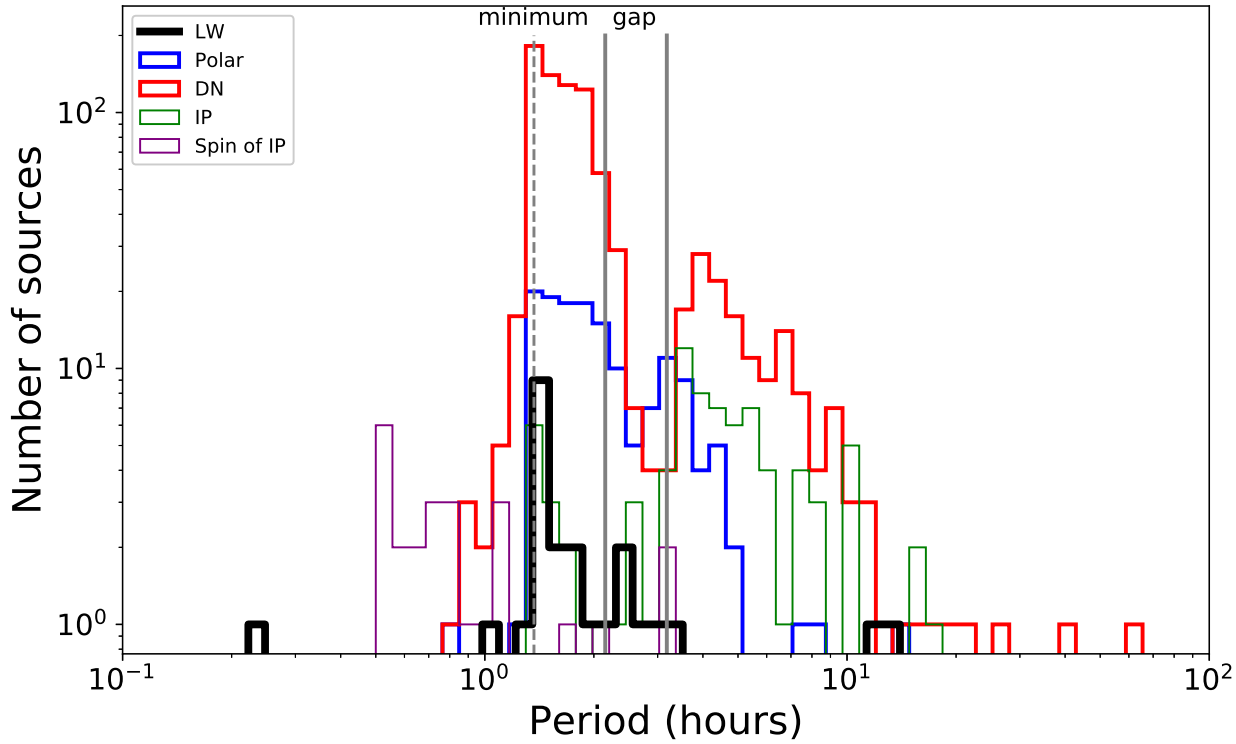

Figure 7. The period distribution of the LW sources (dark-blue line), the spin (purple) and orbital (green) periods of IPs ,the periods (sky-blue) of polars and the orbital (red) periods of DNe from the RK catalog (Ritter & Kolb 2003), version 7.20). The famous period gap(yellow line) and period minimum(orange dashed line) are also plotted, whose value are taken from (Knigge et al. 2011).

corresponding phase-folded light curve is consistent with the one-pole behavior (Figures 4). This is naturally understood in terms of a spin modulation. In the meantime, the phase-folded light curve of #14 shows a dip at phase 0.9–0.1, which may be understood as obscuration by the accretion stream, i.e., an orbital modulation. The corresponding orbital period of 5608.2 sec is reasonable for IPs. The two periods of #21 and #22 differ by only 5% from each other (9877.5 sec vs. 10342.3 sec). The light curve of #22 exhibits a narrow dip near phase 0.5 (Figure 5). This is a clear sign of eclipse when viewed from a high inclination, thus the period of #22 should be the orbital period. On the other hand, the light curve of #21 shows only gentle variation and is best understood as due to spin modulation. Considering that the angle between the magnetic and spin axes (β) is usually small, the moderate variation also makes

sense. In this regard, source #21/#22 is probably an IP or a so-called asynchronous polar.

It is worth asking, if some of the aforementioned sources (#3, #7, #11, #18, #19 and #20) were indeed IPs, why only their orbital period is detected. One plausible explanation is that their spin period, presumably below ∼ 1 hour, escapes detection due to a relatively detection efficiency. Our simulations (3.3) suggest that for moderate total counts and moderate variation amplitude, the detection rate is generally low for short periods. This effect may apply in all those six candidate IPs except #19, which has total counts of 3402. Perhaps this source has a very low spin modulation due to the "one-pole" behavior. One the other hand, source #2, which has not been discussed so far, shows a period of 3820.8 sec, significantly lower than the canonical orbital period minimum (65–82 minutes, determined from observations and binary synthesis modelling, e.g., Gänsicke et al. 2009; Knigge et al. 2011). Thus this period is more likely to be the spin period. In this regard, a spike-like feature in the phase-folded light curve of #2 may be caused by a bright spot on the WD surface. The unseen orbital modulation may be due to a low inclination angle.

In DNe (i.e., non-magnetic CVs), hard X-rays are produced in the boundary layer near the WD surface, in which case spin modulation is essentially absent and orbital modulation is also expected to be weak, unless the inclination angle i is sufficiently large to allow for a total eclipse. Among the 25 periodic signals, no clear sign of total eclipse is seen except for the case of #22. However, we have argued in the above that source #21/#22 is most likely an IP. Therefore, there is probably no DN among the periodic sources. This is consistent with the generally low to moderate detection rates of eclipse based on our simulations in Section 3.3.

Lastly, we remark on the possible non-CV source #25. This source has an unabsorbed 1–8 keV luminosity of 7.5×10^{30} erg s^{-1}, the lowest among all 23 sources. Its X-ray spectra, characterized by a best-fit plasma temperature of 2.3 keV (notably with large uncertainties; Table 3), is also the softest among all sources. These values are more typical of ABs. Moreover, the phase-folded light curve of #25 suggests that the X-ray flux drops to the background level for nearly half of the 47317-sec period (Figure B1). As mentioned in the above, this may be due to a polar producing hard X-rays from only one of its two poles. However, we consider such a case rather unlikely, since the corresponding period is much larger than that of any previous known polars (Figure 7), which would imply for an exceptionally strong magnetic field in the WD. Alternatively and more likely, this can be explained by a total eclipse lasting for half cycle. In this case, the eclipsed star cannot be a WD, because of the mismatch between the stellar radius (order 10^4 km) and the orbital separation (order 10^7 km). Rather, the eclipsed star is likely to have a size not much smaller than the orbital separation, suggesting an AB system viewed nearly edge-on. However, the near-zero flux for half-cycle is unusual for ABs. One possibility is that this system consists of a Sun-like star and an A-star, the latter producing no significant X-rays due to a very weak surface magnetic field (Güdel 2004). An estimated orbital separation of 4 $R_\odot$ from the period is compatible with such a system.

In summary, based on the X-ray properties of the periodic sources, in particular their phase-folded light curves, we identify 13 candidate polars, 2 probable plus 7 candidate IPs, and one probable AB. Admittedly, polars and IPs share similar characteristics in their phase-folded light curves, as described above. The non-detection of the spin period (or orbital period in the case of #2) brings about substantial uncertainty in the IP identification. It is also noteworthy that only two long (> 3.5 hours) periods are found among the 22 orbital periods (3 probable spin periods subtracted). This fraction (∼9%) is significantly smaller than the fraction of long-period CVs in the solar neighborhood (∼??% according to the catalog of Ritter & Kolb 2003, version 7.20). This cannot be due to a selection effect of the GL algorithm, because our simulations in Section 3.3 show that the detection rate is generally higher for longer periods.

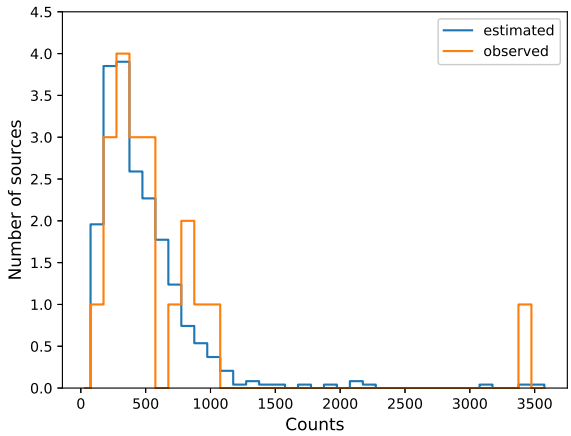

Figure 8. The comparison between estimated and the real detected number of sources.

6.3 CV populations in the Galactic bulge

Firstly, we assumed that the fraction of polars in the total sample of 667 sources is α and the sinusoidal variation happens only in "two-pole" situation, which needs the accretion of polar falls onto one pole and $i+\beta+\epsilon > 90^\circ$. Taking the equal probability hypothesis for parameters and at least half of polars with one-pole accretion, we can set 25% (50% × 50%) as the lower limit of fraction for polars with sinusoidal variation intrinsically. Then we obtain the mean detection rate from simulation, by combining the even distribution for amplitude from 0.5 to 0.9 and the harmonic average for results of P=5540s (60%) and P=45540s (40%). The value of 60% and 40% are estimated from the period distribution beyond and below the gap, respectively. Thus far, we get the detection rate only depended on number of counts. We set width=100 for our binning of counts, from 75 to 3575, covering nearly all detected sources. The predicted number of periodic sources which "should" be detected in each counts bin is calculated by:

$$Np_i = N_i \times DR \times 25\% \times 667 \times \alpha \quad (4)$$

N_i is the number of sources in the bin , i.e, $\sum N_i = 667$. DR denotes the detection rate in this counts bin weighted from simulation. Then we sum all Np_i together and force it equals to 20, getting α about 17%. The value of 20 is taken as the upper limit by considering all periodic sources but three with determined properties (two IPs and one AB). The comparison between Np_i, which denotes the predicted detection and the real detected 20 periodic sources are plotted in Figure 8. The perfect agreement between their population proves the validity of estimation.

Since the real luminosity function should be gentle than that of total sample, which means there could be more polars at the bright band, then it demanding lower numbers of polar to balance the high detection rate for bright sources. Besides, with the intrinsic fraction (25% as the lower limit) increasing, the α decreasing. In general,

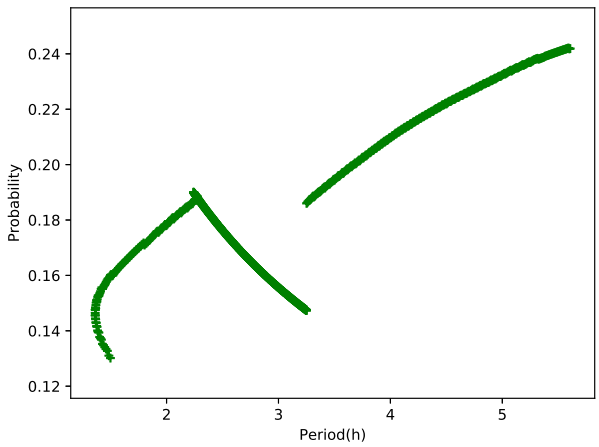

Figure 9. Probability of eclipsing in CVs. The break around 3.2hours resulted by different model for CVs beyond and below the period gap.

the 17% should be treated as the upper limit for polars, especially when we considered all the 20 sources are polars.

The same approach can be applied to IPs by evaluating the detection for spin period. Still, we set 25% (50%×50%) as the lower limit of fraction for IPs with sinusoidal variation intrinsically and gain the detection rate in each counts bin by averaging the simulation results for P=554s. Since only three period are considered as the spin of IP, we set 3 as the upper limit for the value of $\sum Np_i$. Then estimation of the fraction of IPs is about 5%. And it should be taken as the upper limit for similar reasons above.

While for DNe, we are constrained by lack of reliable X-ray luminosity function(XLF). We could set one as the upper limit of DNe since no reliable detections of DNe. However, the steeper XLF for DNe than the XLF for total sample would only contribute the lower limit for their proportion. Though this conflict leads to the uncertainty of estimation, we still present the estimation for fraction of DNe as supplement. Intrinsically, the eclipse of white dwarf depends on the inclination angle, radius of companion star and orbit. If we set i as inclination, R_1,R_2, a as radius of WD, companion star and separation respectively. then eclipsing happens when :

$$a \times cosi \leq R_1 + R_2 \tag{5}$$

Assuming that inclination angle is even distributed in $(0, 90°)$, the probability of eclipsing(hereafter EP) are plotted in Figure 9. The value of R_1, R_2 and a are taken from simulation operated by (Knigge et al. 2011), in which R_1 is fixed at when M_{WD} equals 0.75 solar mass.

We utilized the simulation results of 5258s and 15258s as the detection rate for period under (75% of the total number) and beyond (25% of the total number) the period gap. The fraction is also taken from the statistics as shown in from Figure 7. Besides, EP was chosen as 0.18 and 0.20 for this two types. Similarly, the predicted number of periodic non-mCVs which "should" be detected in each counts bin is:

$$Np_i = N_i \times DR \times EP \times 667 \times \alpha \tag{6}$$

Since the sum of Np_i was assigned as one, the α would be around 0.25 if we set 10^{32} erg s^{-1} (roughly corresponding 675 counts) as the upper limit of luminosity for DNe. The rationality of the limit has been proved by the DNe sample from solar neighborhood in (Xu et al. 2016), based on *Suzaku* observation. The uncertainty of this fraction comes from our limited acquaintance about XLF for DNe, and no detection of periodic DNe.

7 SUMMARY

1. We have discovered 23 periodic sources with 25 signal in the LW by using GL method, including 10 of them already found by LS method in Hong et al. (2012). Their luminosity range locates at 10^{31} – 10^{33} erg s^{-1}.The general feature of these 23 sources resembles that of polars. Two of them are determined as IP.

2. We estimate the mass of WD from a source with great identification for Fe XXVI and Fe XXV emission lines, i.e. 0.8 $M_\odot$ for #21(#22) as being an IP.

3. We provide well-constrained fraction of polars in the whole sample, i.e, 17% as the upper limit. The estimation on fraction of non-mCVs is about 25% while the certainty is restricted by limited appreciation about their XLF. Combined with the period distribution, we conclude that the periodic sources are mainly polars with relatively harder spectra, especially in the luminosity range that lower than 10^{32} erg s^{-1}. Besides, the H sources (L>10^{32} erg s^{-1}), whose emission is mostly contributed by IPs, indicate $M_{WD} \sim 0.8M_\odot$, consistent with the previous result $0.8 \pm 0.07M_\odot$ in (Yu et al. 2018).

4. The lower luminosity and narrow eclipsing model for orbital modulation reduced the detection rate simultaneously for periodicity. That may explain why we had no trace on non-mCVs in GCR in earlier period searching work.

5. We proved the higher detection rate, more usage of data and ignorance of observation gap for GL method compared with LS method. It is noteworthy that the shape of light curve in GL method could be modified according to different scenarios. It was applied on detection of planetary transits by using customized eclipsing model (Aigrain & Favata 2002). For the utility of GL method, there is still room for improvement in the future.

We thank Xiaojie Xu and Zhenlin Zhu for helpful discussions. This work is supported by the National Key Research and Development Program of China under grant 2017YFA0402703.

REFERENCES

Aigrain S., Favata F., 2002, A&A, 395, 625
Buccheri R., et al., 1983, A&A, 128, 245
Cheng Z., Li Z., Li X., Xu X., Fang T., 2019, ApJ, 876, 59
Cicuttin A., Colavita A. A., Cerdeira A., Mutihac R., Turrini S., 1998, ApJ, 498, 666
Deeming T. J., 1975, Ap&SS, 36, 137
Edelson R. A., Krolik J. H., 1988, ApJ, 333, 646
Gänsicke B. T., et al., 2009, MNRAS, 397, 2170
Gregory P. C., Loredo T. J., 1992, ApJ, 398, 146
Güdel M., 2004, A&ARv, 12, 71
Hailey C. J., et al., 2016, ApJ, 826, 160
Heise J., Brinkman A. C., Gronenschild E., Watson M., King A. R., Stella L., Kieboom K., 1985, A&A, 148, L14
Hellier C., 2001, Cataclysmic Variable Stars
Hellier C., Garlick M. A., Mason K. O., 1993, MNRAS, 260, 299
Hong J., 2012, MNRAS, 427, 1633
Hong J. S., van den Berg M., Grindlay J. E., Laycock S., 2009, ApJ, 706, 223

Hong J., van den Berg M., Grindlay J. E., Servillat M., Zhao P., 2012, ApJ, 746, 165
Knigge C., Baraffe I., Patterson J., 2011, ApJS, 194, 28
Leahy D. A., Darbro W., Elsner R. F., Weisskopf M. C., Sutherland P. G., Kahn S., Grindlay J. E., 1983, ApJ, 266, 160
Lomb N. R., 1976, Ap&SS, 39, 447
Morihana K., Tsujimoto M., Yoshida T., Ebisawa K., 2013, ApJ, 766, 14
Muno M. P., Baganoff F. K., Bautz M. W., Brand t W. N., Garmire G. P., Ricker G. R., 2003, ApJ, 599, 465
Muno M. P., et al., 2009, ApJS, 181, 110
Norton A. J., Beardmore A. P., Taylor P., 1996, MNRAS, 280, 937
Revnivtsev M., Sazonov S., Churazov E., Forman W., Vikhlinin A., Sunyaev R., 2009, Nature, 458, 1142
Revnivtsev M., Sazonov S., Forman W., Churazov E., Sunyaev R., 2011, MNRAS, 414, 495
Ritter H., Kolb U., 2003, A&A, 404, 301
Sazonov S., Revnivtsev M., Gilfanov M., Churazov E., Sunyaev R., 2006, A&A, 450, 117
Scargle J. D., 1982, ApJ, 263, 835
Schuster A., 1898, Terrestrial Magnetism (Journal of Geophysical Research), 3, 13
Schwarzenberg-Czerny A., 1996, ApJ, 460, L107
Silber A. D., 1992, PhD thesis, MASSACHUSETTS INSTITUTE OF TECHNOLOGY.
Stellingwerf R. F., 1978, ApJ, 224, 953
Wevers T., et al., 2016, MNRAS, 462, L106
Xu X.-J., Wang Q. D., Li X.-D., 2016, ApJ, 818, 136
Xu X.-J., Li Z., Zhu Z., Cheng Z., Li X.-d., Yu Z.-l., 2019, ApJ, 882, 164
Yu Z.-l., Xu X.-j., Li X.-D., Bao T., Li Y.-x., Xing Y.-c., Shen Y.-f., 2018, ApJ, 853, 182
Zhu Z., Li Z., Morris M. R., 2018, ApJS, 235, 26
van den Berg M., Hong J. S., Grindlay J. E., 2009, ApJ, 700, 1702

APPENDIX A: A BRIEF INTRODUCTION TO THE GREGORY-LOREDO ALGORITHM

The basic rules for Bayesian probabilities are the sum rule,

$$p(H_i|I) + p(\bar{H}_i|I) = 1, \tag{A1}$$

and the product rule,

$$p(H_i, D|I) = p(H_i|I) \cdot p(D|H_i, I) = p(D|I) \cdot p(H_i|D, I). \tag{A2}$$

From Eqn. A2 we can derive Bayes's theorem,

$$p(H_i|D, I) = p(H_i|I) \cdot \frac{p(D|H_i, I)}{p(D|I)}. \tag{A3}$$

The symbols here follow Gregory & Loredo (1992). Specifically, p is the Bayesian posterior probability, H_i denotes the i-th hypothesis, D for the data, and I for the ensemble of all hypotheses, i.e., all the model used. The GL algorithm employs a stepwise function to detect periodic signal. Each model has $(m+2)$ parameters: the angular frequency $\omega = 2\pi/P$ (P is the period), the phase parameter ϕ, and m values of r_j, which denotes the count rate in each phase bin where j=1 to m. In the following we replace H_i by M_i to denote the model where i represents the number of bins in the stepwise model. Then the Bayes's theorem can be written as,

$$p(M_i|D, I) = p(M_i|I) \cdot \frac{p(D|M_i, I)}{p(D|I)}. \tag{A4}$$

We can write $I = M_1 + M_2 + M_3 + \cdots$, where "+" stands for "or". Thus the proposition (M_i, I) is true if and only if model M_i is true, i.e. $(M_i, I) = M_i$. The GL algorithm defines an odds ratio for model comparison,

$$O_{ij} = \frac{p(M_i|D, I)}{p(M_j|D, I)} = \frac{p(M_i|I)}{p(M_j|I)} \cdot \frac{p(D|M_i)}{p(D|M_j)} \tag{A5}$$

Note that M_1 means a constant model, M_i (i=2,3,4...$N_{\rm mod}$, where $N_{\rm mod}$ is the total number of models considered) represents a periodic model. The probability for each model can be deduced from Eqn. A5,

$$p(M_i|D, I) = O_{i1} \cdot p(M_1|D, I), \tag{A6}$$

thus

$$p(M_1|D, I) = \frac{\sum_{j=1}^{N_{\rm mod}} p(M_j|D, I)}{\sum_{j=1}^{N_{\rm mod}} O_{j1}} = \frac{1}{\sum_{j=1}^{N_{\rm mod}} O_{j1}}. \tag{A7}$$

Substituting Eqn. A7 into Eqn. A6, we have

$$p(M_i|D, I) = \frac{O_{i1}}{\sum_{j=1}^{N_{\rm mod}} O_{j1}}. \tag{A8}$$

Then the probability of a periodic signal is

$$p(M_m(m > 1)|D, I) = \frac{\sum_{m=2}^{m_{\rm max}} O_{m1}}{1 + \sum_{m=2}^{m_{\rm max}} O_{m1}}, \tag{A9}$$

where $m_{\rm max}$ is the maximum value of m. The odds ratio can be calculated from the probability of the model,

$$O_{m1} = \frac{p(M_m|D, I)}{p(M_1|D, I)}. \tag{A10}$$

Using Bayes's theorem (Eqn. A4),

$$O_{m1} = \frac{p(M_m|I) \cdot p(D|M_m)}{p(M_1|I) \cdot p(D|M_1)}. \tag{A11}$$

Following the assignment by Gregory & Loredo (1992), we assume that the periodic and aperiodic signals have the same probability. Then the priors for the models can be written explicitly as,

$$p(M_1|I) = \frac{1}{2}, \tag{A12}$$

$$p(M_m|I) = \frac{1}{2\nu}, \quad \nu = m_{\rm max} - 1. \tag{A13}$$

For astronomical data of Poisson distribution, it can be shown that (Equation 5.27 in Gregory & Loredo 1992),

$$p(D|M_m) = \frac{\Delta t^N (m-1)! N! \gamma(N+1, A_{\rm max}) T}{2\pi A_{\rm max} (N+m-1)! T^{N+1} \ln(\omega_{\rm hi}/\omega_{\rm lo})} \times \int_{\omega_{\rm lo}}^{\omega_{\rm hi}} \frac{d\omega}{\omega} \times \int_0^{2\pi} d\phi \frac{m^N}{W_m(\omega, \phi)}, \tag{A14}$$

where $\omega_{\rm lo}$ and $\omega_{\rm hi}$ are the lower and upper bounds of the frequency range. It should be emphasized that the above equation holds for the case in which the period and phase are both unknown. Substituting $m = 1$ into Eqn. A14, we have

$$p(D|M_1) = \frac{\Delta t^N N! \gamma(N+1, A_{\rm max}) T}{A_{\rm max} N! T^{N+1}}. \tag{A15}$$

Substituting Eqns. A12, A13, A14 and A15 into Eqn. A11, the odds ratio can be written as follows, which is the same as Equation 5.28

in Gregory & Loredo (1992),

$$O_{m1} = \frac{1}{2\pi\nu \ln(\omega_{\rm hi}/\omega_{\rm lo})} \binom{N+m-1}{N}^{-1} \times \int_{\omega_{\rm lo}}^{\omega_{\rm hi}} \frac{d\omega}{\omega} \times \int_0^{2\pi} d\phi \frac{m^N}{W_m(\omega,\phi)} \tag{A16}$$

Astronomical data are often subject to observational gaps. This may result in unevenly covered phase bins, leading to spurious detections especially at low frequencies. Gregory & Loredo (1992) provides a solution to this problem, by introducing a weighting factor

$$S(\omega,\phi) = \prod_{j=1}^{m} s_j^{-n_j}, \tag{A17}$$

$$s_j(\omega,\phi) = \frac{\tau_j(\omega,\phi)}{T/m}, \tag{A18}$$

where T is the total time span between the first and last photons and $\tau_j(\omega,\phi)$ denotes the exposure time in each phase bin. Then the odds ratio should be modified as,

$$O_{m1} = \frac{1}{2\pi\nu \ln(\omega_{\rm hi}/\omega_{\rm lo})} \binom{N+m-1}{N}^{-1} \times \int_{\omega_{\rm lo}}^{\omega_{\rm hi}} \frac{d\omega}{\omega} \times \int_0^{2\pi} d\phi \frac{S(\omega,\phi) m^N}{W_m(\omega,\phi)}. \tag{A19}$$

Ultimately, the probability of whether the dataset is periodic is,

$$p(\text{periodic}) = \frac{\sum_{m=2}^{m_{\rm max}} O_{m1}}{1 + \sum_{m=2}^{m_{\rm max}} O_{m1}}. \tag{A20}$$

The posterior probability of the frequency contains the period of the signal,

$$O_{m1}(\omega) = \frac{1}{2\pi\nu} \binom{N+m-1}{N}^{-1} \times \int_0^{2\pi} d\phi \frac{S(\omega,\phi) m^N}{W_m(\omega,\phi)}. \tag{A21}$$

The period locates at $P = 2\pi/\omega$ when $O_{m1}(\omega)$ takes the highest value.

APPENDIX B: ADDITIONAL FIGURES OF THE PERIODIC X-RAY SOURCES

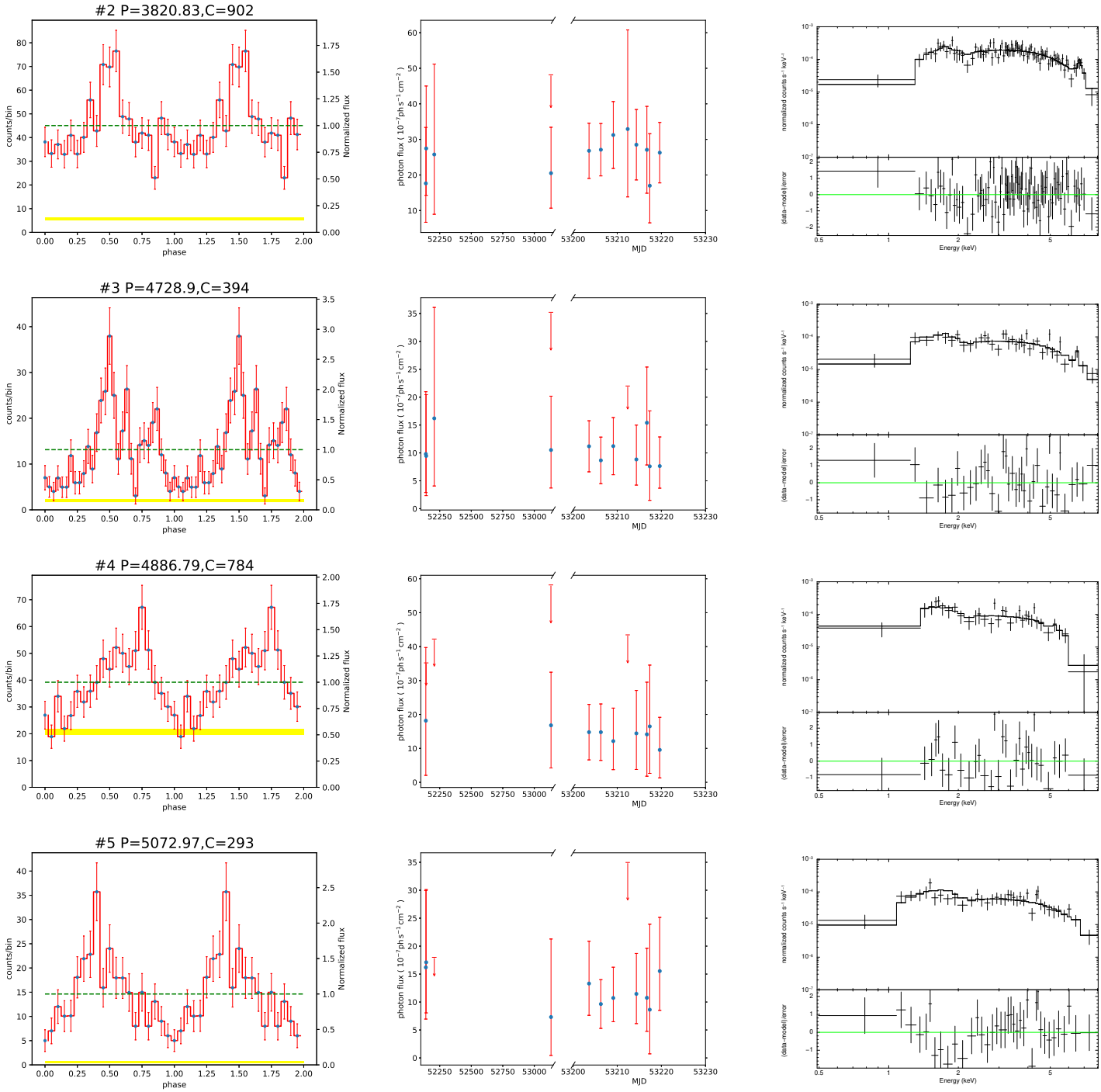

Figure B1. The phase-folded light curve (left) , the long-term, inter-observation light curve (middle) and the spectra (right) for all the source in Table 2, similar to Figure 4.

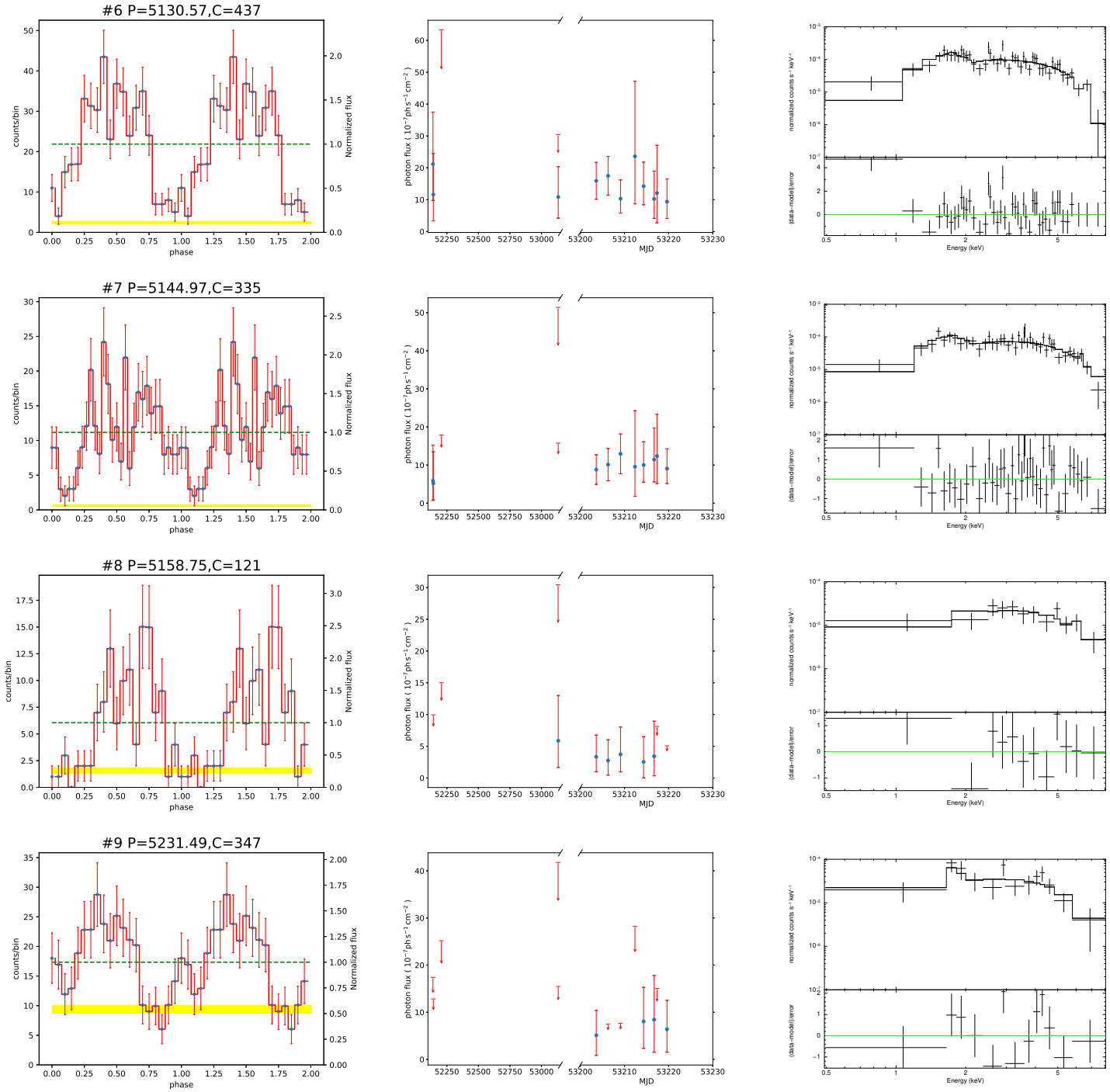

Figure B2. First figure continued

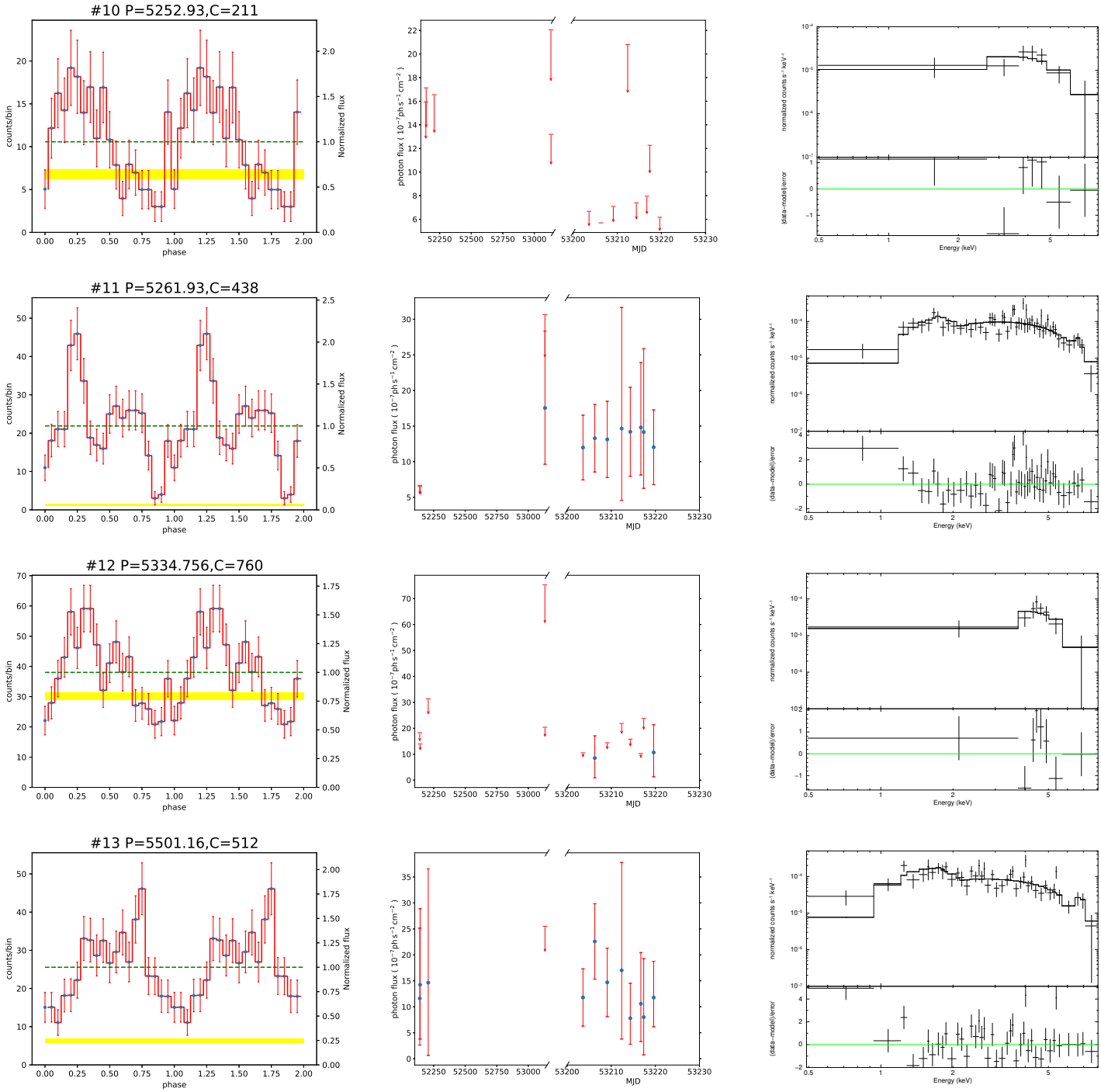

Figure B3. First figure continued

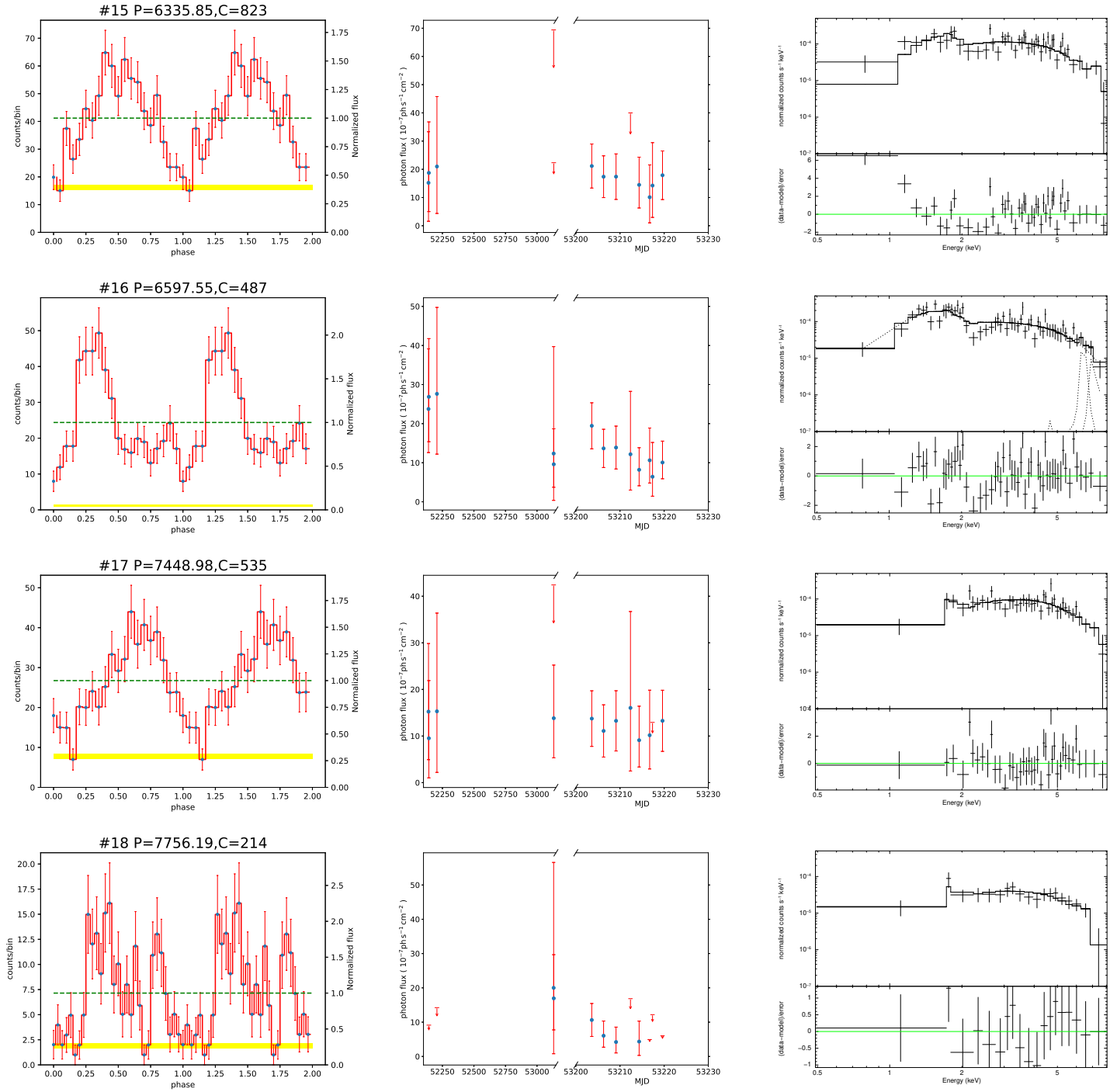

Figure B4. First figure continued

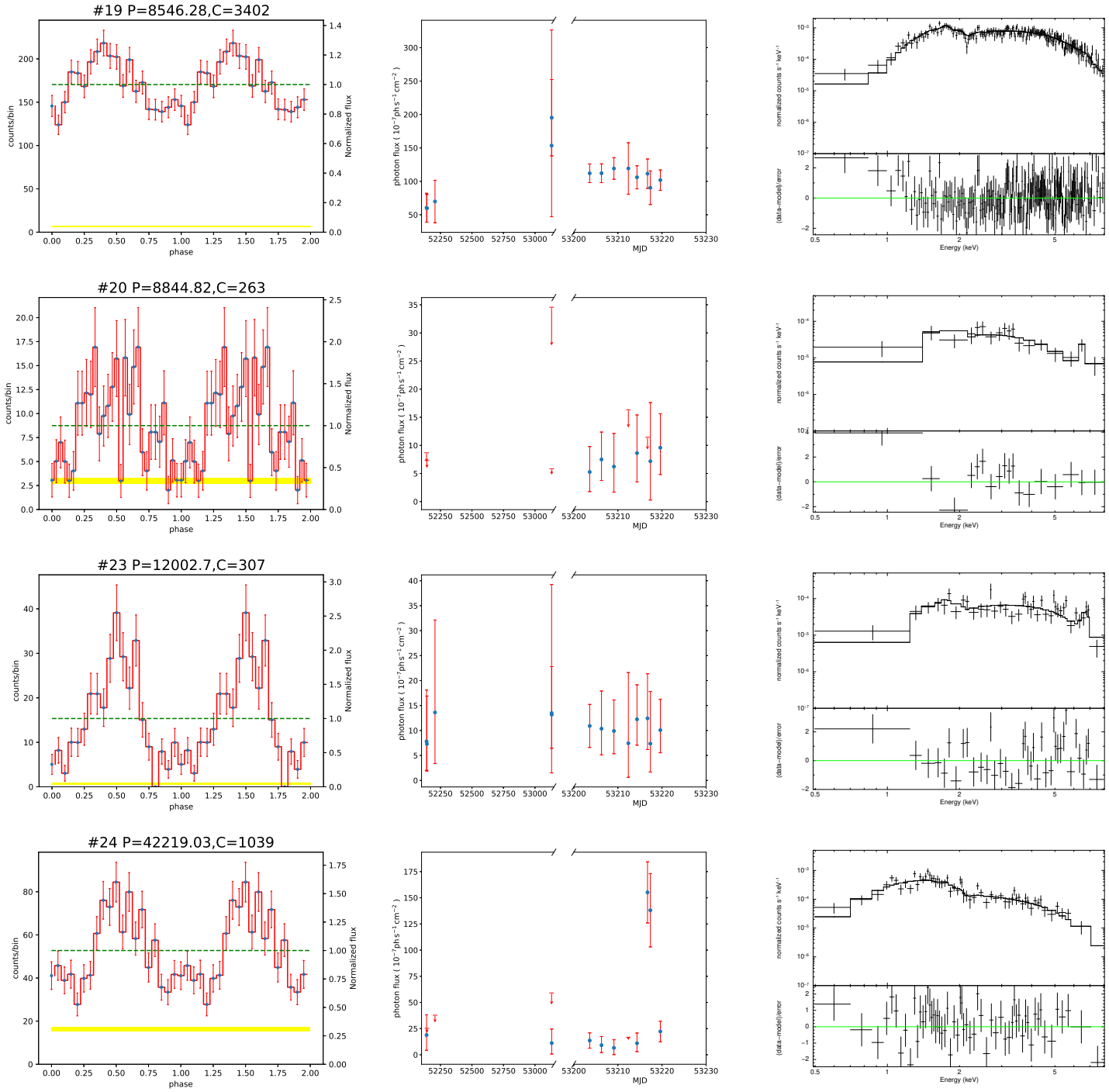

Figure B5. First figure continued

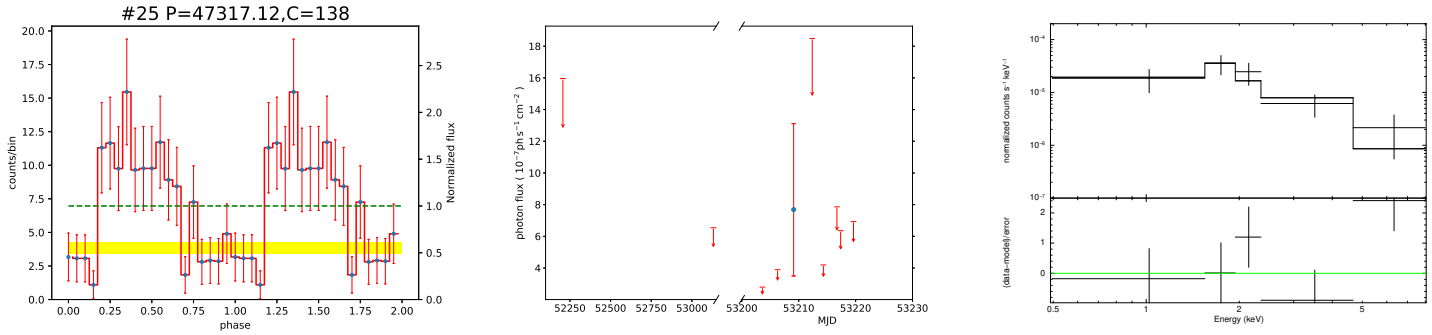

Figure B6. First figure continued